

Measurement of the continuum of dimuons produced in high-energy proton-nucleus collisions

A. S. Ito,* R. J. Fisk,* H. Jöstlein,* and D. M. Kaplan†
State University of New York, Stony Brook, New York 11794

S. W. Herb, D. C. Hom,‡ L. M. Lederman, H. D. Snyder,§ and J. K. Yoh
Columbia University, New York, New York 10027

B. C. Brown, C. N. Brown, W. R. Innes,|| R. D. Kephart, K. Ueno, and T. Yamanouchi
Fermi National Accelerator Laboratory, Batavia, Illinois 60510
 (Received 4 April 1980)

We report final results of a series of measurements of continuum dimuon production in proton-nucleus collisions at Fermilab. New results with 6 times more statistics are included. A full description of the apparatus and methods used in the analysis of this series of measurements is given. The sea quark distribution of the nucleon is determined within the context of Drell-Yan and quantum-chromodynamic descriptions of dilepton production in hadron collisions.

I. INTRODUCTION

In the past ten years advances in the constituent theory of hadrons have been paced by developments in three experimental areas: inelastic lepton-nucleon scattering (using e^+ , μ^+ , and ν 's), e^+e^- annihilation, and dilepton production in hadron-hadron collisions:

$$h_1 + h_2 \rightarrow l^+ + l^- + \text{anything} . \tag{1}$$

Reaction (1) has been further exploited to find new massive resonances ($J/\psi, \Upsilon$) in addition to probing the details of hadronic substructure in a manner which is complementary to the scattering approach. This paper is based upon proton-induced-dimuon research carried out at Fermilab. We summarize the previously published results¹⁻⁵ and present a final analysis representing a sixfold increase in data. Extended descriptions of the apparatus, systematic effects, and corrections are also given.⁶ We concentrate here on the continuum of massive $\mu^+\mu^-$ pairs produced as in Eq. (1); our final results on the Υ family of resonances observed via their decay to the $\mu^+\mu^-$ final state have been published elsewhere.⁷

The data discussed in this paper are divided into three sets: I. 400 GeV incident proton energy; II. 200/300 GeV; III. 400 GeV (high intensity). In addition, we will present some previously unpublished dielectron data.

Analysis of the data from reaction (1) has been carried out using the Drell-Yan parton-antiparton annihilation model,⁸ which was proposed to describe the first such data obtained at the Brookhaven Alternating Gradient Synchrotron (AGS).⁹ In this model a quark (antiquark) constituent in a beam nucleon and an (antiquark) constituent in a beam target nucleon annihilate via a virtual photon into a lepton pair. The remaining quarks go off into

the "anything" of Eq. (1). This is shown schematically in Fig. 1. Thus the cross section for producing a dilepton of mass m is proportional to a sum of terms of the form

$$f(x_1)\bar{f}(x_2), \tag{2}$$

where $f(x)/x$ ($\bar{f}(x)/x$) is the probability to find a quark (antiquark) bearing the fraction x of the hadron's momentum. Annihilation kinematics give

$$\tau \equiv m^2/s = x_1x_2, \tag{3}$$

where s is the nucleon-nucleon center-of-mass energy squared. The structure functions f and \bar{f} also appear in lepton scattering. The dilepton data therefore test the consistency of the model. Moreover, in dilepton production the antiquark distribution (a measure of the quark-antiquark sea) appears as a multiplicative factor in the product rather than as an additive term (as in lepton-nucleon scattering) and so is more sensitively measured. The detailed expression for the cross section is

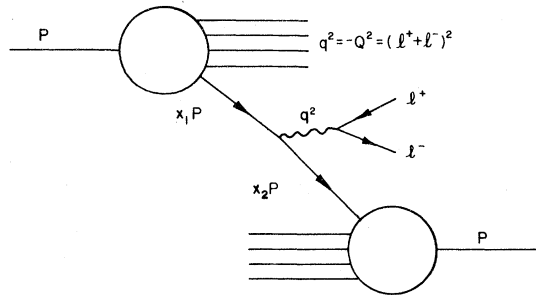


FIG. 1. Basic Drell-Yan process; a parton-antiparton pair annihilate via a virtual photon into a pair of leptons.

$$m^4 \frac{d\sigma}{dm^2} = \frac{4\pi\alpha^2}{9} \sum_i e_i^2 \int_0^1 \int_0^1 \{ dx_b dx_t [f_i^b(x_b) \bar{f}_i^t(x_t) + \bar{f}_i^b(x_b) f_i^t(x_t)] \delta(\tau - x_b x_t) \}, \quad (4)$$

where $t \equiv$ target nucleon, $b \equiv$ beam nucleon, and $e_i \equiv$ charge of i th quark. The sum is over the quark flavors u, d, s, c , etc., except that it is customary to neglect the c and heavier quarks because of their mass. Equation (4) contains the concept of scaling, i.e., $m^4 d\sigma/dm^2$ depends only on τ . There is an important factor-of-3 decrease in the cross section due to the color degree of freedom. This is one of the very few places where one can "see" this hidden quantum number, and its testing in this reaction could provide an important confirmation of the color concept. The test clearly involves an appeal to the lepton scattering data for normalized structure functions $f_u \equiv u(x)$, $f_d \equiv d(x)$, $f_s \equiv s(x)$, $\bar{f}_u \equiv \bar{u}(x)$, etc., in the same kinematic regions and a prescription for how to go from space-like Q^2 to timelike m^2 .

Dilepton production has more recently come in for great theoretical attention because of two observed features which are not included in the Drell-Yan model: (i) the dileptons have transverse momenta which are much larger than the typical hadronic p_T of 300 MeV/c,⁴ and (ii) the nucleon structure functions, measured in muon-nucleon scattering,¹⁰ violate scaling. These developments are understood within the context of quantum chromodynamics (QCD), a quantum field theory of quark-quark interactions. In this theory quarks and antiquarks coupled by neutral vector particles (gluons) are the fundamental constituents of the hadrons. The modification of the Drell-Yan model by the additional diagrams of QCD has occupied a substantial fraction of the literature.¹¹⁻²⁰ The reason is twofold: (i) dilepton data provide a testing ground for perturbative calculations in the new theory, and (ii) the data may permit an over-determination of parameters which are not as yet fixed by the theory. We shall return to these issues after a lengthy excursion into experimental matters.

II. EXPERIMENTAL DETAILS

A. General

The experiment measures the vector momenta of two opposite-sign leptons emerging from the hadronic collision, \vec{P}_+ and \vec{P}_- . From this, the relevant kinematical quantities may be deduced. Assuming $|\vec{P}_+|, |\vec{P}_-| \gg m_\mu$ ($m_\mu \equiv$ mass of the muon),

$$m^2 = 2 |\vec{P}_+| |\vec{P}_-| [1 - \cos(\theta_{+-})], \quad (5)$$

$$y = \frac{1}{2} \ln \frac{E^* + P_{\parallel}^*}{E^* - P_{\parallel}^*}, \quad (6)$$

where θ_{+-} , P_{\parallel}^* , and E^* are the angle between the two muons in the laboratory, the dimuon longitudinal momentum, and the dimuon energy in the nucleon-nucleon center-of-mass (c.m.) system, respectively. The c.m. rapidity y is related to the Bjorken x variables defined in Fig. 1 in the following manner:

$$\begin{aligned} x_1 &= \sqrt{\tau} e^{+y}, \\ x_2 &= \sqrt{\tau} e^{-y}. \end{aligned} \quad (7)$$

We note that these relations are strictly valid only in so far as $m \gg p_T \equiv$ dimuon transverse momentum and $\sqrt{s} \gg m_n \equiv$ nucleon mass.

B. Design criteria

We wished to measure the lepton-pair continuum out to the highest possible masses, and also to be sensitive to massive resonances. To improve on previous continuum measurements we needed to be sensitive to cross sections less than 10^{-12} of the total proton-nucleon cross section, and therefore to take a large incident-beam flux and to withstand high counting rates in the apparatus. Good mass resolution was particularly important for the resonance search; good resolution in other variables minimized corrections to the observed data. Since massive objects tend to be produced at rest or moving slowly in the collision rest frame, we chose to view the collision at 90° , thus avoiding the huge hadronic flux at 0° and 180° .

We had the choice of detecting muons or electrons. Muons can be distinguished from the copiously produced hadrons by their highly penetrating character; electrons, by their electromagnetic showering properties. The main background in a muon experiment is muons from the decay of pions and kaons produced in the target. To suppress this it is necessary to place material immediately downstream of the target to absorb these particles before they can decay. The advantage over electrons is that the particle flux is in principle lowered by a factor of up to 10^4 by the hadron absorber, allowing a corresponding increase in beam intensity. The disadvantage is that scattering of the muons in the hadron absorber degrades knowledge of their production angles, thus worsening resolution. Electron pairs were detected in the earliest arrangement.¹ A preliminary muon experiment was performed² using an apparatus very similar to that of the electron experiment. Insertion of beryllium hadron absorber for the muon test run lowered counting rates in the apparatus by a

factor of about 4, rather than 10^4 . Hadronic cascades in both the beryllium and the forward beam dump generated large numbers of low-energy muons which contributed random-singles rates in all detector planes, preventing a large increase in the proton-beam intensity.

The experience gained allowed us to optimize the design of the present experiment, improving both sensitivity and resolution. The crucial regions around the target and beam dump were redesigned to minimize the decay muon flux; this decreased the rate per incident proton by about a factor of 10. We had also noted from the previous experiment that the muon flux did not decrease rapidly with distance from the magnets. Therefore, the acceptance was enlarged without increasing counting rates by moving all detectors closer to the target and analyzing magnets. Acceptance was also gained by permitting bends of either sign in each spectrometer arm. These improvements permitted an overall increase in data taking rates of more than a factor of 60 over the previous muon experiment.

C. Apparatus overview

The apparatus (shown in Fig. 2) was a two-arm magnetic spectrometer viewing the proton-nucleus collision from opposite sides at $\sim 90^\circ$ in the proton-nucleon center-of-momentum system (c.m.s.). Each arm covered a solid angle of 0.2 sr in the c.m.s. and consisted of hadron absorber, two magnets, scintillation counters, and multiwire proportional chambers (MWPC's). The magnets deflected charged particles vertically and in opposite directions, so that if the first (air-gap) magnet deflected positive muons up, say, the second (solid-steel) magnet deflected them down. Each arm was symmetric about a horizontal plane and accepted both positive and negative muons equally.

To maximize the amount of beam we could ac-

cept, we placed no detectors upstream of the air-gap magnet where counting rates were at least an order of magnitude higher than downstream. The momentum was computed from the measured trajectory downstream of the air magnet by assuming that the undeflected track pointed back to the target. The inaccuracy of this assumption due to multiple scattering in the hadron absorber resulted in a rms momentum resolution of 2%.

The spectrometer apertures were wide horizontally and short vertically. The fields in the two air-gap magnets were oriented along the long dimension of the gaps. The muon production angles were thus measured primarily in a plane perpendicular to the plane of magnetic deflection. This decoupling of the production-angle measurement from the momentum measurement had important advantages over the more usual magnet design in which the field is oriented along the short dimension. First, the copious low-momentum muons were swept out of the spectrometer, rather than being swept across the aperture into the other arm. Second, events originating in upstream vacuum windows or in the beam dump could be rejected by projecting the track back to the target in the horizontal plane.

In order to suppress backgrounds, the apparatus was designed with a considerable amount of redundancy. The momentum of the muon was redetermined to $\pm 15\%$ by measurement of the deflection in the steel magnet. This helped to reject low-energy muons which simulated high-momentum muons by traversing the air magnet along strange trajectories involving scattering from pole pieces, return yokes, etc. Another handle on backgrounds was provided by the midmagnet (MM) MWPC which verified the muon position in the middle of the air magnet. A gas Čerenkov counter filled with nitrogen provided a 4-GeV muon energy threshold, as did the energy loss in the 1.8 m of

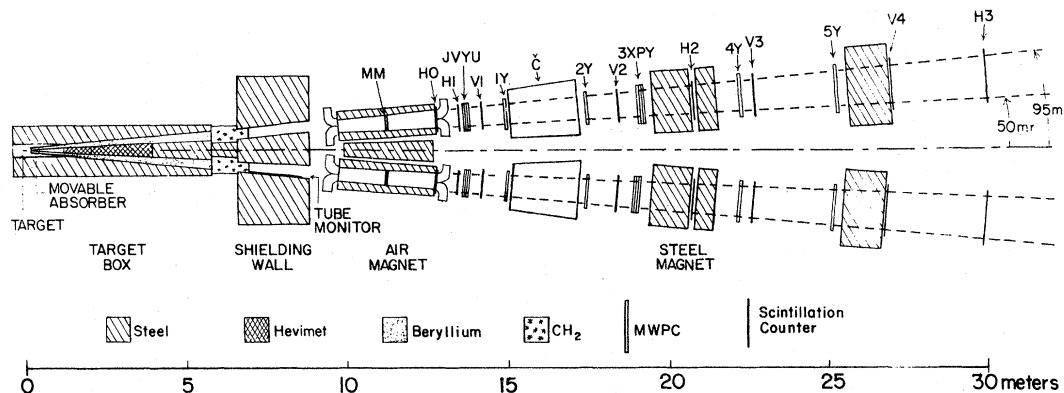


FIG. 2. Schematic plan view of the two magnetic spectrometers used to measure the yield of muon pairs. The various detector stations are described in the text.

steel magnet and 1 m of steel further downstream. At full current the magnets provided a 15-GeV threshold for particles traversing all the detectors, but the Cerenkov counter and additional steel were still useful in eliminating certain classes of "junk" triggers such as accidental coincidences of low-energy muons upstream and downstream of the steel magnet.

The detector system included both scintillation counters and multiwire proportional chambers at most positions after the analyzing magnets. Counters were used to create the event trigger; matrix logic requirements for counter hodoscopes in both the bend and nonbend planes provided crucial reductions in the trigger rate.

The external beam at Fermilab arrives in bursts (rf buckets) of about 1 nsec duration and separated by 18.9 nsec. Resolution of single buckets is easily achieved with scintillation counters, but proportional chambers integrate over two or three buckets. The scintillation-counter hodoscopes were therefore also used to eliminate out-of-time chamber hits during the off-line reconstruction.

D. Detailed description

The apparatus is here described in detail proceeding from upstream to downstream.

1. Beam line

The experiment (E288) was performed in the proton-center pit of the Fermi National Accelerator Laboratory. A small fraction of the extracted primary proton beam was brought to the proton-center pretarget area by switchyard and proton-area

magnets mostly not under our control. The protons were steered and focused onto our target by two dipole and five quadrupole magnets which we could control using the MAC beam-line computer system. We were able to focus the beam to a spot 0.03 cm by 0.08 cm high [full width at half maximum (FWHM) as measured during the Columbia-Fermilab-Stony Brook (CFS) hadron-pair experiment²¹]. The horizontal and vertical beam profiles 0.7 m upstream of our target were measured by 0.5-mm-spacing separated-wire ionization chambers (SWIC's) provided by Fermilab research services. A secondary-emission monitor was used to measure the beam intensity.

2. Target box

The target box (Fig. 3) was a large helium-filled enclosure containing ten drawers, on which were mounted the target holder, beam dump, and part of the hadron absorber. The drawers were 1 ft square in cross section and were arrayed five across and two deep; they slid in and out on rails. Surrounding the target box was a 16-in.-thick layer of steel to shield against radioactivity.

3. Targets

Four different targets were used. The targets were thin vertical strips of metal with a horizontal width of about 1 mm. This defined the horizontal interaction position precisely and also minimized the scattering of outgoing muons. The vertical size of the interaction region was determined by the natural beam height of about 2 mm. Most of the data were taken with either a 1.87-cm-long

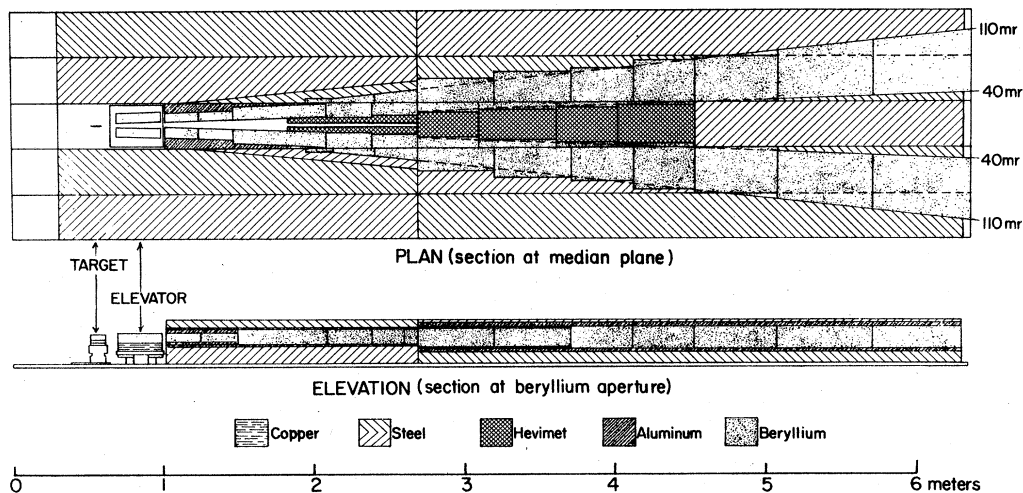


FIG. 3. Target-shielding box containing ten removable carriages on which were housed the target, beam dump, and aperture defining beryllium channels.

platinum target or a 10-cm-long Cu target. These targets were chosen in order to maximize the ratio of signal to single count rates, since the massive lepton-pair signal had been measured to have an approximately linear nucleon-number (A) dependence while the singles rate presumably goes as $A^{2/3}$ (see Sec. III B 3(b) below). During the data taking to measure the A dependence, we alternated frequently between the platinum target and a 10-cm-long beryllium target. The fourth target was the 7-cm-long copper target, which was used during a small fraction of the run. The targets were mounted in a holder which could be translated horizontally (transverse to the beam direction) by means of a stepping motor under computer control. Target parameters are given in Table I.

4. Beam dump

Typically, 30–50% of the beam interacted in the target; the rest was absorbed in a water-cooled beam dump. The dump began 210 cm downstream of the center of the target. It consisted of 180 cm of Mallory 1000 Hevimet (90% tungsten, 6% nickel, 4% copper) followed by 6 ft of steel. A cone of Hevimet extended 90 cm upstream to reduce the decay path for hadrons produced at small angles, but it had a 2.5-cm-square hole in its center to allow the unscattered beam to pass through. Hevimet was used for its short hadronic absorption length (11 cm), which minimizes decay of pions and kaons and also minimizes the transverse spread of the hadronic shower and hence leakage of particles out of the dump into the aperture.

5. Targeting monitors

The fraction of the beam intercepted by the target was monitored by two different methods. A 2.5-cm-diameter hole in the steel shielding directly above the target provided a decay space for hadrons emitted upwards, and the resulting muon flux was viewed (after penetration of the concrete pre-target-area roof and some dirt) by a four-element scintillation-counter telescope

called the 90° monitor. This was our main targeting fraction monitor. The 90° monitor was somewhat sensitive to interactions in the dump; typically the ratio of its “target-in” to “target-out” counting rates was about 4. A second targeting monitor was a single-wire proportional tube counter called the tube monitor; it viewed the target from the large-angle side of the aperture in one arm and had a target in/target out ratio similar to that of the 90° monitor.

6. Hadron absorber

In the laboratory rest frame each spectrometer arm covered ± 10 mrad vertically and 45 mrad horizontally. The two arms were centered horizontally on the angles $\pm (\arctan 0.0725)$, which correspond to $\sim \pm 90^\circ$ in the c.m.s. at 400 GeV beam energy. Within the target box the spectrometer apertures were filled with hadron absorber, the first 30 cm of which sat on a remotely controlled elevator platform which could be raised or lowered to have copper, beryllium, or no absorber (i.e., helium) in the aperture. Almost all of our data were taken with the copper absorber, as we found that rates in some of the detectors increased by as much as a factor of 3 with beryllium; the small improvement in resolution with beryllium (see Sec. E below) was judged not to be worth the accompanying beam-intensity limitation. The rest of the absorber consisted of 525 cm of beryllium in the target box and 150 cm of CH_2 downstream of the target box.

The beryllium was oversized, its coverage being nowhere less than 70 mrad horizontally, nor ± 20 mrad vertically. This provided a buffer zone of low- Z material around the nominal aperture so that muons scattering in the Hevimet or steel of the target drawers could not be confused with the muons produced within the aperture. The beryllium was in the form of large precisely cut blocks in order to minimize gaps. Similar precautions extended to the surrounding steel and to the beam dump. The design benefited from our previous ex-

TABLE I. Target properties. Length of Pt target is given as measured after run. Widths and densities of Pt and Be were measured using leftover pieces from the same sheet-metal stock.

Material	Length (cm)	Width (mm)	A	Density (g/cm^3)	Absorption lengths	Effective lengths (cm)
Pt	1.87 ± 0.04	0.660 ± 0.013	195.09	20.65 ± 0.40	0.2	1.70 ± 0.04
Be	10.38 ± 0.10	1.65 ± 0.13	9.01	1.835 ± 0.014	0.28	9.04 ± 0.09
Cu	7.62	0.889	63.54	8.96	0.52	5.94
Cu	10.16	0.889	63.54	8.96	0.69	7.35

perience in the detection of massive muon pairs and from a detailed Monte Carlo study. The effort in careful redesign of the target box was rewarded by a factor of ~ 10 improvement in random-singles rates in the downstream detectors.

The CH_2 was included because of the worry that slow neutrons might be able to penetrate the beryllium in significant numbers and contribute to counting rates. Subsequent running failed to support this view, however, and after a few months of running all but 15 cm of the CH_2 was removed and 138 cm of beryllium installed in its place.

7. Shielding wall

Three feet downstream of the end of the target box was a 210-cm-thick steel shielding wall. The apertures in this wall were slightly oversized. They were tapered horizontally, but not vertically. The tube monitor was placed in the downstream end of the down-arm shielding-wall aperture in the lower large-angle corner.

8. Air-gap magnets

Next came the air-gap analyzing magnets. They were 300-cm-long dipole magnets centered 11 m downstream from the center of the target. The field was horizontal (deflecting charged particles vertically), and, due to tapering of the gaps, the field decreased in magnitude with increasing distance from the target. The pole pieces were located at 49 and 97 mrad. At maximum current (1500 A) the mean value of the field was 13 kG, giving a transverse momentum kick of 1.2 GeV/c. The two magnets were wired in series. Their fields pointed in the same direction, so that if positive particles were deflected up in one arm, negative particles were deflected down in the other; this configuration favors pairs produced at small transverse momentum and thus has larger acceptance than the configuration in which the fields are directed oppositely.

The field integral of each magnet, as a function of the horizontal (x) and vertical (y) coordinates in each arm, was mapped at several currents using a 450-cm-long flip coil connected to a current integrator, and the magnitude of the field at the upstream end near the 49-mrad pole piece was measured continuously to 0.2% by a Hall-effect probe. The magnet current was monitored using a precision shunt which was sensitive to 0.1% current variations. A second current shunt was read back from the power supply via the controls computer system. A further check on the shape and magnitude of the field was the observed mass of the J/ψ resonance as a function of current and position in the magnet. We also used the J/ψ reso-

nance to calibrate the field near the pole pieces where flip-coil measurements were difficult.

9. Detectors

Table II lists the detectors, in the order traversed by a muon. The first detector in each arm was an MWPC (2-mm-spacing horizontal wires) located in the center of the air magnet. These midmagnet (MM) chambers were designed to operate efficiently at the high counting rates (typically 50 MHz) encountered in that location. Their narrow gaps ($\frac{1}{8}$ in.) reduced the time spread of pulses from a single track to about 50 nsec, and special dead-time-less amplifier-discriminator cards were used. All MWPC's used a gas mixture containing 83% argon, 17% CO_2 , and 0.1% freon 13B1. Most of the chambers were operated at high rates (10–20 MHz/plane) for several years without changes in plateau voltages or need for repairs. The MWPC electronics was of the standard "Nevis" design,²² except for the Sippach-designed fast amplifier-discriminators mentioned above.

Four stations of detectors were placed between the air magnet and the steel magnet. The first station consisted of a plane of horizontal scintillation counters designated $H1$, a MWPC containing three planes of wires (2-mm spacing) designated as J chambers, and a vertical scintillation-counter hodoscope known as $V1$. $H1$ was used in the trigger. The three J chambers (JY , JU , and JV) mea-

TABLE II. Detectors.

Name	Type	z position (in.)	
		Up arm	Down arm
MM	MWPC	440.0	440.0
$H0$	hodoscope	500.0	500.0
$H1$	hodoscope	529.0	529.0
JV	MWPC	537.6	537.9
JY	MWPC	538.6	538.9
JU	MWPC	539.6	539.9
$V1$	hodoscope	558.8	555.6
$1Y$	MWPC	588.1	588.1
C	Čerenkov		
$2Y$	MWPC	688.0	688.0
$V2$	hodoscope	724.0	724.0
$3X$	MWPC	745.1	745.2
$3P$	MWPC	750.6	750.7
$3Y$	MWPC	756.1	756.2
$H2$	hodoscope	817.0	817.0
$4Y$	MWPC	875.0	875.0
$V3$	hodoscope	893.0	893.0
$5Y$	MWPC	990.6	990.6
$V4$	hodoscope	1056.5	1053.0
$H3$	hodoscope	1173.0	1173.0

sured in the y direction and along two axes at 60° and 120° from the y axis. $V1$ consisted of 19 1.4-in.- and 2-in.-wide scintillation counters. It supplemented the MWPC's in measuring x , and its good time resolution (one accelerator rf bucket) permitted elimination of out-of-time MWPC hits. A second plane of horizontal scintillation counters called $H0$ was added upstream of $H1$ after a few months of running. It consisted of five 5-cm-wide strips fit snugly against the downstream face of the magnet iron, restricting the trigger to muons emerging from the magnet aperture and eliminating the roughly 30% of pair triggers due to muons emerging through the coils.

The next station consisted of a single 2-mm-spacing MWPC measuring y and called 1Y. Between it and the third station was a 210-cm-long nitrogen-filled Čerenkov counter. It was the "head" section of a nitrogen Čerenkov counter C2, used in the previous hadron-pair experiment.²¹ It was used in the muon experiment primarily for its good time resolution (1 nsec rms) and also for its insensitivity to slow particles.

The third station was a 3-mm-spacing MWPC measuring y and called 2Y. The fourth station consisted of a vertical hodoscope of 26 1.4-in.- and 2-in.-wide scintillation counters, called $V2$, and three 3-mm MWPC's (3Y, 3X, and 3P) measuring y , x , and a coordinate (p) rotated by $\arctan(\frac{1}{8})$ with respect to y . The preponderance of chambers measuring y (and p , which is highly correlated with y) was intended to provide accurate measurement of the magnetic deflection angle even if one or two chambers should be missing due to inefficiency.

10. Steel magnets

Figure 4 shows a steel magnet in detail. Each steel magnet was made of nine 8-in.-thick steel slabs welded together into a 4-ft. section followed by a 24-in. section, separated by ~6-in. space. The coil consisted of 36 turns of hollow 0.825-in.-by-0.625-in. water-cooled copper. The magnet was run at a current of 1000 A, which was suffi-

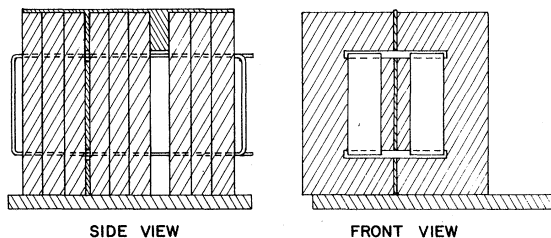


FIG. 4. Detail of solid-steel magnets used to reanalyze the muon momentum and harden the trigger.

cient to saturate the steel at approximately 20 kG and provide a fairly uniform dipole field. The field integral was measured using the muons themselves, studying the distribution in deflection angle as a function of momentum measured by the air magnet. The transverse-momentum kick p_T was thus measured to be 1.14 GeV. The two magnets were wired in series and the current monitored to 0.1% by a precision shunt. Their fields were equal and oriented in the same direction, opposite to the direction of the fields in the air magnets. Muons were thus partially refocused by the steel magnets, allowing downstream detectors to be reduced in size.

The momentum resolution of such a magnet is limited by multiple scattering of the muons as they traverse the steel. The rms scattering angle is given by²³

$$\theta_{\text{rms}}^2 = \left(\frac{0.014 \text{ GeV}}{p} \right)^2 \frac{L}{R} \left(1 + \frac{1}{9} \log_{10} \frac{L}{R} \right)^2, \quad (8)$$

where p is the muon momentum, L is the length of the magnet, and $R = 1.77$ cm is the radiation length of steel.²⁴ The magnetic deflection angle θ_{bend} also depends inversely on the momentum and is given in the small-angle approximation by

$$\theta_{\text{bend}} = p_T/p = 1.14 \text{ GeV}/p. \quad (9)$$

Thus the rms momentum resolution is given by

$$\frac{\sigma_p}{p} = \frac{\theta_{\text{rms}}}{\theta_{\text{bend}}} = 0.15. \quad (10)$$

This was entirely adequate for the task of rejecting background events (see Sec. III D).

11. More detectors

In the space between the two sections of each steel magnet was a plane of horizontal scintillation counters ($H2$). It consisted of four counters each 8 in. wide, with the upper and lower of the four angled so that the vertical aperture was larger at large horizontal angles than at small ones. Since low-momentum muons were deflected through large angles in the air magnet, they tended to be at the upper and lower edges of $H2$, so the tapering of $H2$ provided some rejection of low-transverse-momentum muons (and hence of low-mass pairs).

Following the steel magnet were two 3-mm MWPC's with horizontal wires designated 4Y and 5Y, and a vertical scintillation hodoscope ($V3$) made of nine 12-cm-wide strips. Following 41 in. of steel (to further "harden" the trigger against low-momentum muons) were a vertical hodoscope ($V4$) made of 13 15-cm-wide strips overlapped to give 5-cm resolution, and the final trigger plane

H3, consisting of four 20-cm-wide horizontal scintillation counters.

E. Resolution

1. Calculated resolution

Each spectrometer arm measured angles to a precision limited by chamber-wire spacings and by multiple scattering in the hadron absorber. The contribution of wire spacing to angle-measurement error is straightforward. The multiple-scattering contribution can be computed from

$$\theta_{\text{rms}}^2 = \left(\frac{0.016 \text{ GeV}}{p} \right)^2 \frac{L}{R}, \quad (11)$$

where

θ_{rms}^2 = projected mean-square scattering angle,

p = muon momentum,

L = length of absorber,

R = radiation length of absorber material.

For the sake of simplicity, this formula differs from the formula (8) above in that this is the appropriate form for very thin absorber, for which the logarithmic correction term is negligible. Since, however, it is to be integrated over thick absorbers, the constant has been increased appropriately. Calculation of the resolution in variables of physical interest is complicated because integrations must be done over the actual event distribution in the other variables and also because the resolution varies from event to event depending on which chambers participate in the reconstructed track. Figure 5 shows the results of a detailed analytical calculation of the mass resolution. In this calculation, the effects of multiple scattering and MWPC measurement errors are evaluated for their influence on both momenta and opening angles.

2. Mass resolution from data

The expected mass resolution can be computed more exactly using the events themselves, since then the distribution of events in the apparatus and chamber inefficiencies are taken correctly into account. The analysis program propagates errors through the track reconstruction and mass calculation, yielding the expected mass error for each event. The points shown in Fig. 5 represent the 1500 A mass resolution thus computed, averaged over 1 GeV mass intervals. It is seen to agree with the analytic calculation given above within 5%.

We have verified that these resolution calculations are correct by studying the J/ψ . For this purpose, we took special runs at air-magnet cur-

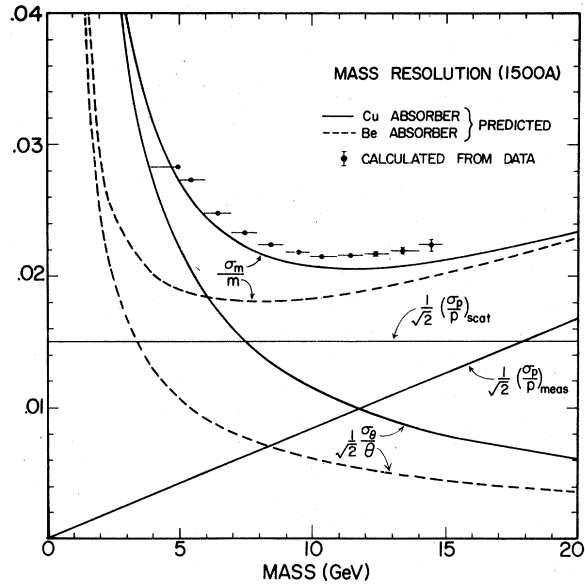


FIG. 5. Mass resolution of the dual spectrometers at full excitation. The various calculated contributions to the resolution are explained in the text along with the event-by-event resolution calculated from the data.

rents of 750, 1000, and 1250 A, since the J/ψ has too low a mass to be accepted significantly by the spectrometer at a current of 1500 A. For these runs we used beryllium as the first foot of absorber. The mass distributions are shown in Fig. 6. Table III compares the calculated mass resolution with the observed width of the J/ψ . The agreement is good at all three currents.

This agreement tests the multiple-scattering component but, because of the low momenta, does not adequately test the measuring error. Here we appeal to data on target size as obtained from reconstructed tracks. This is shown in Fig. 7 in various mass bins where the data are contrasted with the expected distribution obtained from a

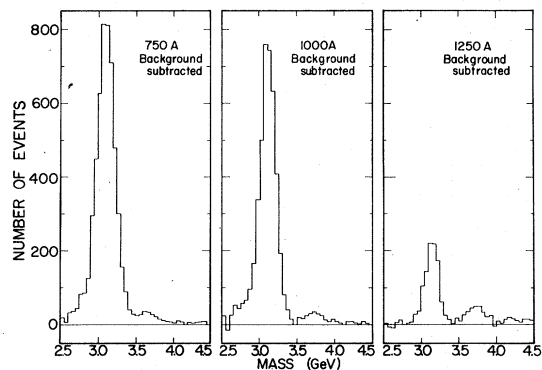


FIG. 6. Mass-resolution plots in the region of the J/ψ resonance taken at lower magnet excitation.

TABLE III. J/ψ resolution.

Current (A)	Predicted (GeV, FWHM)	Observed
750	0.275	0.277
1000	0.227	0.251
1250	0.195	0.204

Monte Carlo program. The agreement is convincing evidence that our resolution is well understood.

F. Trigger

In data sets I and II, the trigger for each arm consisted of the coincidence of $H0$, $H1$, $H2$, $H3$,

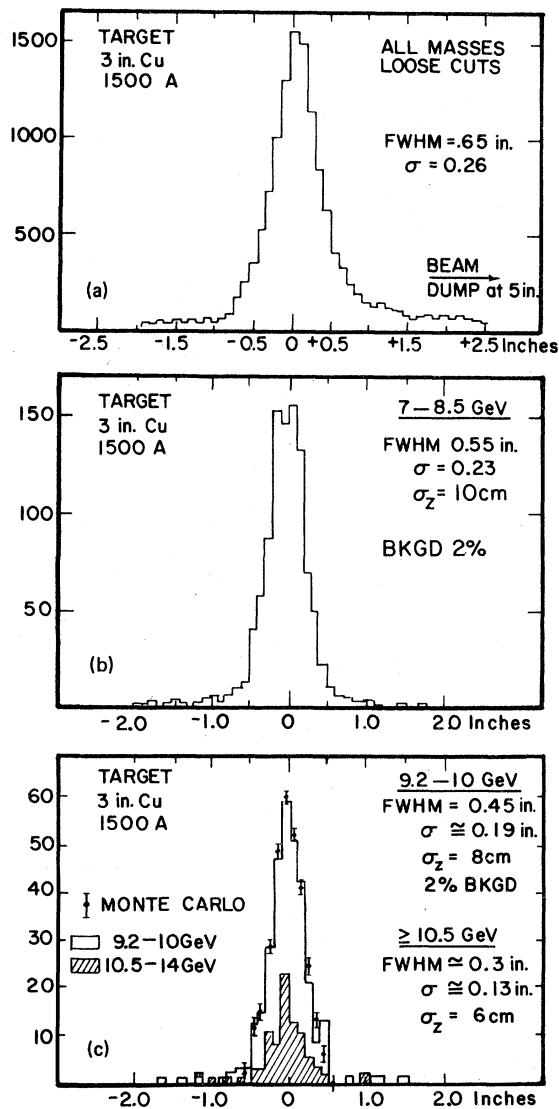


FIG. 7. Reconstructed target distribution in a coordinate perpendicular to the beam for (a) all masses, (b) masses 7–8.5 GeV, (c) masses 9.2–10 GeV and 10.5–14 GeV.

$V2$ and the matrix $V1 \times V4$. This matrix formed rough roads, selecting muons coming directly from the target in the horizontal plane. In data set III, matrices $H0 \times H9$ and $H2 \times H3$ (forming roads in the vertical plane) were added to the coincidence requirement. For the high-intensity runs of set III we also required that less than four hits occur in the $V2$ hodoscope. This served to veto accidental coincidences generated by large fluctuations in beam intensity. In addition to these primary triggers, prescaled study triggers were simultaneously taken in order to monitor the efficiency of the system. Typically, a study trigger did not require some element and a comparison of the study trigger and the event trigger yielded the efficiency of the element in question. The data-taking rate of the study triggers was carefully chosen to allow the entire surface of all detector elements to be tested with good statistical accuracy. The overall trigger efficiency averaged 90%.

Intensities of the incident-proton beam were adjusted so that in general singles counting rates in the most burdened detector (typically less than 20 MHz) did not result in dangerous inefficiencies. Triggers were refined until the rates were 100–200 per machine pulse. The vast majority of triggers were arm-to-arm accidentals and so the quality of the data was highly dependent upon the performance of the accelerator. The quality of the micro and macro structure of the Fermilab accelerator spill was continually evaluated by the on-line computer and fed back to the accelerator control room as a television display. The details of the data-acquisition system are presented in Appendix A.

III. DATA REDUCTION

A. General; efficiencies

The first stage of the analysis was data compression. Its aim was to reduce some 1000 data tapes to a manageable number in a reasonable amount of computer time. There were four levels of compression, called A, C, D, and E. In the A level, a simple track-finding algorithm was used to compute the invariant mass of the muon pair. Events failing this algorithm were eliminated. All subsequent analysis used the more complicated "standard" track-reconstruction algorithm.

Subsequent levels of compression eliminated events failing the standard reconstruction algorithm or failing a progressively more stringent series of requirements which were intended to eliminate background events while retaining good efficiency for genuine massive muon pairs. Events

TABLE IV. Sample-selection requirements.

(1) 1 track found in each arm.
(2) ≥ 6 chambers participating in each track.
(3) Track confidence-level cut: If 6-chamber track C. L. ≥ 0.021 . If 7-chamber track C. L. ≥ 0.011 . If 8-chamber track C. L. ≥ 0.001 .
(4) Fiducial cuts.
(5) Muon cuts: ≥ 5 out of (4Y, 5Y, H2, H3, V3, V4) within 3σ of extrapolated track.
(6) Target cut: projected horizontal position at target ≤ 0.3 in. $+20/p$.

were required to pass track-quality, fiducial-volume, and muon cuts.

Track-quality cuts included requirements on the confidence level of the least-squares fit to the track and on the number of chambers participating in the fit.

The muon cuts used information from the detectors behind the steel magnet to confirm the muon momentum as measured by the air magnet. Since hadrons and electrons had been suppressed by a factor of over 10^8 by the 18.5 hadronic absorption lengths of material in the target box, the major remaining background was low-momentum muons appearing to have high momentum due to traversal of the air magnet along unorthodox paths. The reconstructed track was extrapolated through the steel magnet using the momentum measured in the air magnet. At each of 4Y, 5Y, H2, H3, V3, and V4, the distance of the extrapolated track from the nearest active hodoscope element or MWPC wire was computed and compared with the expected rms deviation due to multiple scattering in the steel (and MWPC measuring error in the case of 4Y and 5Y). If the distance was less than three standard deviations the cut was passed. Events were required to pass five out of the six muon cuts. The complete set of cuts as applied to the final sample of events is listed in Tables IV and V. The cuts used and the resulting compression

TABLE V. Fiducial cuts for data sets I and II.

Position	x limits (in.)		y limits (in.)	
Magnet entrance	-8.80	8.80	-5.00	5.00
Magnet exit	-11.80	11.80	-5.00	5.00
H1	-12.50	12.50	-5.90	5.90
JY	-12.25	12.25	-6.30	6.30
V1	-13.15	14.05	-7.50	7.50
Y1	-14.00	14.00	-7.56	7.56
Y2	-16.00	16.00	-11.34	11.34
V2	-18.63	19.13	-16.50	16.50
3Y	-18.00	18.00	-14.17	14.17
H2	-19.00	19.00	-17.00	17.00
Y4	-22.50	22.50	-16.54	16.54
V3	-24.13	24.13	-16.50	16.50
Y5	-27.00	27.00	-17.00	17.00
V4	-27.00	27.00	-16.50	16.50
H3	-28.00	28.00	-17.00	17.00

factor at each level of compression are given in Table VI.

The final stage of compression was the writing of a "data-summary tape" (DST) of events from the E-level compressed tape. The final event sample included events missing up to two chambers and failing any one muon cut, so the efficiency of each chamber and each muon cut could be determined. Events satisfying the study triggers but failing the event trigger allowed determination of the trigger efficiency.

The compression efficiency was found to be $(96 \pm 1)\%$. The reconstruction efficiency was determined by combining the measured individual plane inefficiencies with the reconstruction requirements and found to be $(94 \pm 2)\%$. The overall efficiency was $(77 \pm 6)\%$. See Table VII for a summary of inefficiencies in the A -dependence data.

B. Normalization and corrections

1. General

In order to compute the differential cross sections, we need to know the apparatus accep-

TABLE VI. Levels of compression.

Level	Requirements ^a	Comments	Compression factor
A	Crude reconstruction prescale $m < 3.8$ GeV	800 to 1600 bits per in.	7
C	Standard reconstruction No. of chambers ≥ 6 , $y_{\max} < 5.4$ in.		5
D	$m > 4.8$, C.L. $> 10^{-5}$ if 6 chambers	Scalers to 25 words	3
E	$y_{\max} < 5.2$ in., 4Y or 5Y within 3σ	Scalers to 7 words	3

^a y_{\max} is the maximum vertical excursion of the track in the air magnet.

TABLE VII. Efficiency summary (*A*-dependence data).

	Pt target	Be target
Trigger	0.884 ± 0.051	0.933 ± 0.038
Compression	0.956 ± 0.014	0.963 ± 0.013
Reconstruction	0.937 ± 0.021	0.951 ± 0.019
Muon cuts	0.990 ± 0.002	0.987 ± 0.002
Target cut	0.988 ± 0.005	0.972 ± 0.008
Track C.L.	1.000 ± 0.002	1.000 ± 0.003
One track	0.990 ± 0.004	0.993 ± 0.003
Combined	0.767 ± 0.057	0.814 ± 0.045
Average	0.796 ± 0.035	

tance and efficiency and the total flux of incident protons. The acceptance is defined as the fraction of muon pairs emerging from the target which traverse the spectrometer. The efficiency is the fraction of pairs traversing the spectrometer which are recorded by the electronics and pass the various analysis cuts. The differential cross section in a bin Δm , Δy , of mass and rapidity is then given by

$$\frac{d^2\sigma}{dm dy} \cong \frac{\Delta\sigma}{\Delta m \Delta y} = \frac{N_{ev}}{N_{inc}} \frac{A}{N_0 \rho L_{eff}} \frac{1}{\epsilon \eta} \frac{1}{\Delta m \Delta y} C, \quad (12)$$

where

- N_{ev} = number of events in the bin $\Delta m \Delta y$,
- N_{inc} = number of incident protons,
- A, ρ, L_{eff} = atomic weight, density, effective length of target,
- N_0 = Avogadro's number,
- ϵ = efficiency,
- η = acceptance in the bin $\Delta m, \Delta y$,
- C = correction factors for nuclear and radiative effects.

The effective length of the target is the length corrected for absorption of the incident beam; it is thus given by

$$L_{eff} = \lambda(1 - e^{-L/\lambda}), \quad (13)$$

where

- λ = hadronic absorption length of target material,
- L = length of target.

The remainder of this section discusses the factors which enter into Eq. (12).

2. SEM calibration

The number of incident protons was measured by a secondary-emission monitor (SEM). The

SEM was calibrated by inserting copper foils into the beam line and measuring the yield of ^{24}Na per SEM count. Assuming that the ^{24}Na production cross section is 3.5 mb per Cu nucleus,²⁵ the SEM calibration constant was found to be $(1.01 \pm 0.02) \times 10^8$ protons per SEM count.

3. Nuclear effects

Equation (12) gives the cross section per atomic nucleus of target material. To get the cross section per nucleon we might divide by A , but this is not necessarily the cross section that would be observed on hydrogen for three reasons: (i) our targets contain neutrons, (ii) the target nucleons are not at rest within the target, and (iii) the cross section might not depend linearly on A . The mix of neutrons and protons is handled by defining an average "nucleon" which, in the case of copper is 60% neutron and 40% proton. In the detailed evaluation of structure functions, use is made of SU(2) symmetry in unfolding the neutron and proton contributions. Below, we discuss the remaining nuclear effects.

(a) *Fermi motion.* Nuclear motion modifies the dimuon yields because of the strong energy dependence of the cross section. Some proton-nucleon collisions have more energy in the c.m. and some have less. The form of the energy dependence is such that cancellation is imperfect and a small correction results. Corrections were made by a Monte Carlo calculation. A simple Fermi gas model²⁶ with a maximum momentum of 260 MeV was used and the sensitivity checked by also using an experimentally determined Fermi-momentum distribution.²⁷ The results differed by less than 20%. The major effect of the Fermi motion is a mass-dependent correction to the spectrum which can be expressed (averaged over the y acceptance)

$$\left(\frac{d^2\sigma}{d\sqrt{\tau} dy} \right)_{\text{corr}} / \left(\frac{d^2\sigma}{d\sqrt{\tau} dy} \right)_{\text{uncorr}} = 0.901 + 0.827\sqrt{\tau} - 2.54\tau. \quad (14)$$

The rapidity- (y) dependent correction is presented in Table VIII. Another effect of nucleon motion is to shift the observed y distribution by an amount $\Delta y = 0.1\sqrt{\tau}$, where

$$E \frac{d^3\sigma}{dp^3} \Big|_y (\text{corr}) = E \frac{d^3\sigma}{dp^3} \Big|_{y+\Delta y} (\text{uncorr}). \quad (15)$$

This is accompanied by a slight loss of resolution in y (0.02, rms) and in p_T (0.03 GeV, rms). These latter effects are not significant.

(b) *A dependence.* An A dependence given by $\sigma \propto A^{2/3}$ would be expected (and has been observed)²⁷ for the bulk of hadronic scattering cross sections; these are the "soft" collisions in which

TABLE VIII. Fermi-motion correction.

$\frac{\left(\frac{d^2\sigma}{d\sqrt{\tau} dy}\right)_{\text{corr}}}{\sqrt{\tau}} \bigg/ \frac{\left(\frac{d^2\sigma}{d\sqrt{\tau} dy}\right)_{\text{uncorr}}}{\sqrt{\tau}} = B_0 + B_1 y + B_2 y^2 + B_3 y^3$	$10^4 B_0$	$10^4 B_1$	$10^3 B_2$	$10^3 B_3$
0.547-0.620	5949	1774	-1280	-2071
0.500-0.547	6831	1652	-659	-1546
0.450-0.500	7506	1711	-225	-1760
0.386-0.450	8199	1060	-68	-944
0.332-0.386	8701	712	-5	-519
0.300-0.332	8973	519	26	-353
0.250-0.300	9218	375	36	-231
0.211-0.250	9407	266	34	-147
0.185-0.211	9517	199	36	-110
0.168-0.185	9582	164	29	-81

little momentum is transferred from the beam particle to the target particle. Such a dependence can be understood in terms of "shadowing" of nucleons inside the nucleus by nucleons on the surface: The incident hadron does not penetrate very far into the nucleus (note that a platinum nucleus is about 3 nuclear collisions lengths thick) and so does not see the nucleons in the interior.

What has been said above implies that all hadronic scattering cross sections should have an $A^{2/3}$ dependence. However, faster A dependences may occur if (as seems to be the case) hadrons have internal structure. Then some components of hadrons (the ones responsible for soft collisions) might interact before reaching the interior of the nucleus, while other components which interact less strongly might see all of the nucleons and interact with linear A dependence. In the parton model, soft processes are due to the interaction of "wee" partons. Wee partons carry a tiny fraction of the momentum of their hadrons, so wee partons from the beam and target move slowly with respect to each other and interact with large probability and $A^{2/3}$ dependence. By contrast, within this model, particles of large transverse momentum and pairs of large mass are produced in collisions of "hard" partons, which carry significant fractions of the momenta of their hadrons. Hard

partons from the beam and target move very rapidly with respect to each other in high-energy collisions and so interact rarely. Their interactions should thus exhibit linear A dependence.

Stronger than linear A dependence has also been observed, both for the production of single hadrons at large p_T ,²⁸ and for hadron pair production at large mass.²⁹ The mechanisms responsible for this are not understood. There is then the possibility that A dependence reflects some subtle and possibly interesting physics involving the behavior of quarks inside a nucleus.

To investigate the A dependence, we took a set of data runs using both platinum and beryllium targets, switching targets every few runs. We parametrize the A dependence by the functional form

$$\sigma \propto A^\alpha \quad (16)$$

and determine the exponent α according to the formula

$$\alpha = \frac{\ln(\sigma_{\text{Pt}}/\sigma_{\text{Be}})}{\ln(A_{\text{Pt}}/A_{\text{Be}})} \quad (17)$$

The relative normalization of the two data samples depends only on the amount of incident flux in each data sample and the targeting fractions for the Pt and Be targets. All other factors cancel since the two samples were taken with the same apparatus and during the same period of time.

The beam targeting efficiencies for the two targets were carefully measured by observing the ratio of the 90° monitor counts divided by the SEM as a function of horizontal target position. The beryllium target was sufficiently wide to intercept all of the beam. The platinum targeting fraction was 0.927 ± 0.073 .

The incident flux was measured by the SEM. The flux factor for each data sample is [from Eq. (12)] $N_{\text{inc}} L_{\text{eff}}$. The flux calculation is summarized in Table IX.

The values for α versus mass and transverse momentum are given in Table X and Fig. 8. The data are consistent with a constant value of α in our mass and transverse-momentum range. Av-

TABLE IX. A -dependence flux calculation.

	Pt target	Be target
SEM counts	12 667 101	23 516 602
90° mon counts	1 808 764	1 698 489
90° live-time gated	1 721 082	1 634 927
Live time	0.9515	0.9626
Incident protons	1.217×10^{15}	2.286×10^{15}
Flux factor	4.274×10^{16}	3.793×10^{16}
Pt/Be flux ratio	1.126 ± 0.035	

TABLE X. α dependence vs mass and transverse momentum. Errors are statistical only. There is an additional 0.028 systematic error at all masses and transverse momenta. The number of doubly charged events is a measure of the background and is subtracted from the number of neutral events in computing α .

Mass (GeV)	Charge		0		2		α
	No. events	Pt	No. events	Pt	No. events	Pt	
5.0- 5.4	146	8	142	4	0.986 ± 0.041		
5.4- 5.8	120	2	115	0	0.994 ± 0.043		
5.8- 6.2	95	0	95	2	0.993 ± 0.048		
6.2- 6.6	87	0	68	0	1.066 ± 0.053		
6.6- 7.0	67	0	63	0	1.006 ± 0.057		
7.0- 7.4	44	0	44	0	0.986 ± 0.069		
7.4- 7.8	35	0	34	0	0.995 ± 0.078		
7.8- 8.2	23	0	24	0	0.972 ± 0.095		
8.2- 8.6	20	0	9	0	1.246 ± 0.131		
8.6- 9.0	11	0	7	0	1.133 ± 0.157		
9.0- 9.4	24	0	18	0	1.079 ± 0.101		
9.4- 9.8	20	0	19	0	1.003 ± 0.104		
9.8-10.2	9	0	8	0	1.024 ± 0.158		
10.2-10.6	2	0	9	0	0.497 ± 0.254		
10.6-11.0	3	0	4	0	0.892 ± 0.248		

p_t (GeV)	Charge		0		2		α
	No. events	Pt	No. events	Pt	No. events	Pt	
0.0-0.2	35	0	49	1	1.089 ± 0.073		
0.2-0.4	120	2	107	1	0.951 ± 0.044		
0.4-0.6	127	2	124	1	0.981 ± 0.042		
0.6-0.8	105	1	102	0	0.980 ± 0.046		
0.8-1.0	90	0	93	1	0.993 ± 0.049		
1.0-1.2	69	1	84	4	1.039 ± 0.055		
1.2-1.4	44	0	50	0	1.027 ± 0.067		
1.4-1.6	28	0	37	1	1.068 ± 0.083		
1.6-1.8	17	0	26	2	1.098 ± 0.107		
1.8-2.0	10	0	12	0	1.045 ± 0.139		
2.0-2.2	8	0	9	0	1.024 ± 0.158		
2.2-2.4	4	0	6	0	1.118 ± 0.210		
2.4-2.6	5	0	2	0	0.688 ± 0.272		

eraging over mass and transverse momentum, we obtain

$$\langle \alpha \rangle = 1.007 \pm 0.018 \pm 0.028, \quad 5 < m < 11 \text{ GeV} \quad (18)$$

where the first error is statistical and the second is systematic (due chiefly to the uncertainty in the platinum targeting fraction).

4. Radiative corrections

Radiative corrections change the shape and the normalization of the continuum mass spectrum. This takes place through the emission of photons and the consequent reduction of the mass of the muon pair. We follow the calculations of Soni³⁰ and find that we can parametrize the result by the form

$$\left(\frac{d^2\sigma}{dm dy} \right)_{\text{corr}} / \left(\frac{d^2\sigma}{dm dy} \right)_{\text{uncorr}} = e^{0.0046(m+0.95 \text{ GeV})}. \quad (19)$$

C. Acceptance

The horizontal acceptance of each arm extended from 50 to 95 mr in the laboratory (0 mr being the beam direction). For light particles and 400 GeV beam energy, this corresponds to 70° to 110° in the proton-nucleon center of mass. For lower beam energies the acceptance moves forward in the center-of-mass frame. The vertical acceptance was a function of momentum, approaching ±10 mr at high momenta. At 72.5 mr horizontal angle, this corresponds to an azimuthal acceptance of ±138 mr in the center of mass.

The pair acceptances are calculated by integrating over irrelevant variables by the Monte Carlo method. In calculating the acceptance for the invariant cross section $E d^3\sigma/dp^3$ at fixed mass, the only nontrivial variables are the muon pair decay (spherical) angles θ_D and ϕ_D . In general, the decay angle distribution can depend on four density-

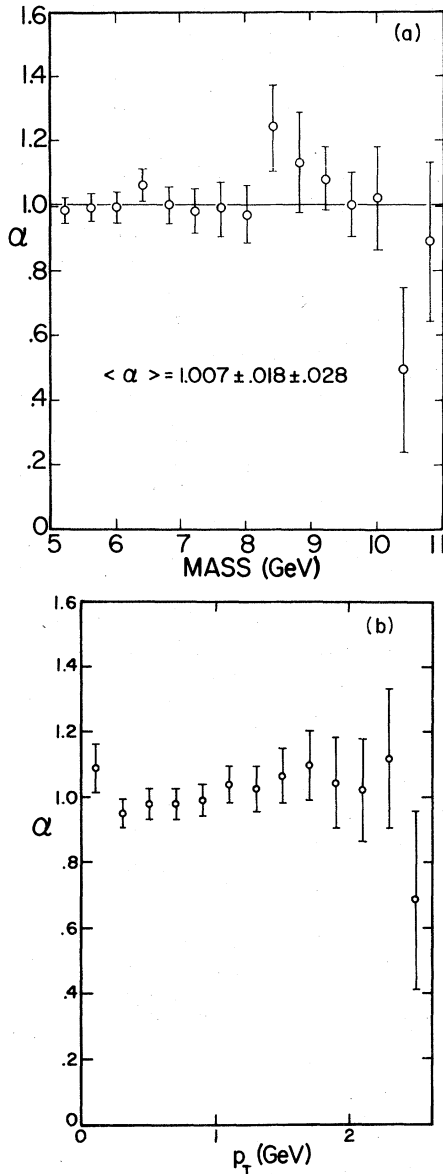


FIG. 8. A-dependence power α , derived from the platinum- and beryllium-target data runs. (a) A dependence of the dimuon yield versus mass (integrated over all p_T). (b) A dependence versus p_T (integrated over all masses).

matrix elements each of which is a function of four invariants.³¹ For some processes, and for appropriate choice of reference-frame orientation, the distribution reduces to the form

$$W(\theta_D, \phi_D) \propto 1 + \delta \cos^2 \theta_D. \quad (20)$$

For example, in the Drell-Yan model the distribution is $1 + \cos^2 \theta_D$ in the frame whose z axis lies along the directions of motion of the (colinear) quark and antiquark (the "quark-antiquark frame").

This presumably is modified somewhat by QCD corrections. If, on the other hand, the intermediate state were an unpolarized particle the decay would be isotropic.

Detailed discussions of the decay angular distribution can be found in the literature.³² For the continuum analysis we have assumed that the Drell-Yan prediction is correct. This has been shown to be true in the experiments of Childress *et al.*³³ and Hogan *et al.*³⁴ in a kinematic range relevant to this experiment. In our experiment, in the quark-antiquark or any closely related frame, the acceptance is restricted to a small range of $\cos \theta$ near 0. Therefore the acceptance ambiguity introduced by uncertainty in δ cannot be resolved within this experiment, but is just one of overall normalization. For simplicity we have chosen to do our calculation in the frame determined by the incident proton (the "Gottfried-Jackson" frame of our previous publications, also called the t -channel helicity frame); such a choice avoids the ambiguity of specifying a partition of p_T between the quark and antiquark as is required to define the quark-antiquark frame. For reasonable partition assumptions the acceptance thus calculated is the same to within a few percent as the acceptance calculated in the quark-antiquark frame. The acceptance calculated using a $1 + \cos^2 \theta_D$ distribution is 0.78 of that calculated using an isotropic distribution, independent of y and nearly independent of p_T .³⁵ The acceptance vs p_T for data sets I and II under the assumption of $1 + \cos^2 \theta_D$ decay is shown in Fig. 9(a).

To obtain the acceptance for the cross section $d^2\sigma/dm dy$, it is necessary to integrate over the p_T of the pair. We did so using the p_T distribution determined from our measured invariant cross sections. These were fit with the form

$$E \frac{d^3\sigma}{dp^3} \propto \frac{1}{[1 + (p_T/p_0)^2]^6}. \quad (21)$$

A typical value for p_0 was 2.8 GeV. This form was also used to extrapolate to p_T 's for which we had no data. The fraction of the integral in this region was typically 1%. Detailed fits using this form have already been presented in Ref. 5. We discuss this further in Sec. IV E.

The acceptance vs center-of-mass rapidity (y) is shown in Fig. 9(b). The y acceptance for three energies is shown in Fig. 9(c). Note that the acceptance peaks near $y=0$ for 400 GeV incident protons and shifts to forward y for lower energies. Since the y acceptance is narrow we present cross sections differential in rapidity evaluated at the mean rapidity of the acceptance $\langle y_{acc} \rangle$. The values of $\langle y_{acc} \rangle$ for the three beam energies are indicated in Fig. 11. The observed rapidity interval at each

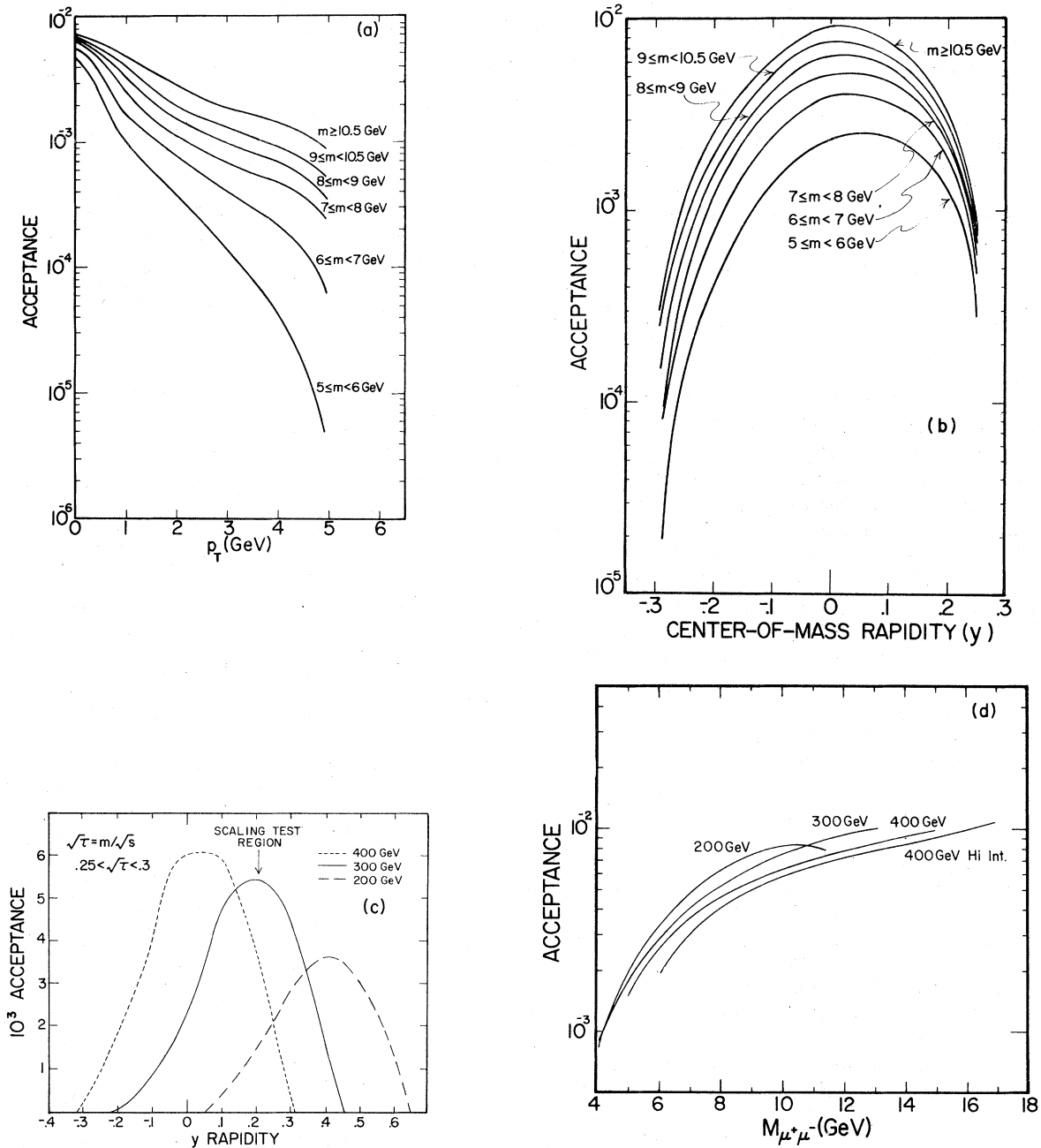


FIG. 9. Dimuon acceptance of the apparatus calculated on the assumption of a $1 + \cos^2 \theta$ decay angular distribution with respect to the beam axis and phenomenological y and p_T production distributions which approximate the data. (a) Acceptance for data set I vs p_T of the dimuon pair, at 400 GeV, (b) acceptance for data set I versus center-of-mass rapidity y of the dimuon pair, at 400 GeV, (c) acceptance for data sets I and II versus c.m. rapidity y of the dimuon pair for 3 energies, (d) acceptance vs mass for the different incident energies.

energy is $\langle y_{acc} \rangle \pm 0.3$. The acceptances versus mass calculated for these intervals are shown in Fig. 9(d). All figures show "observed" y , uncorrected for Fermi motion.

D. Backgrounds

Having evaluated all the terms in Eq. (12), we now discuss the background events included in the

accepted data sample. Backgrounds can come from directly produced muons from two different interactions in the target (accidentals) or from the decays of hadrons. The latter can be from the same or different interactions. We estimate most of these backgrounds with our simultaneous measurement of the $\mu^+\mu^+$ and $\mu^-\mu^-$ rates. If the backgrounds are of accidental origin, whether directly produced or from hadron decays, they obey the relation

$$N_{+-}^{\text{back}} + N_{-+}^{\text{back}} = 2(N_{++}N_{--})^{1/2}. \quad (22)$$

Since in our case $N_{++} \cong N_{--}$, this simplifies to

$$N_{+-}^{\text{back}} + N_{-+}^{\text{back}} \cong N_{++} + N_{--}. \quad (23)$$

We observed that $(N_{++} + N_{--}) / (N_{+-} + N_{-+})$ was proportional to beam intensity in our data. This implies that indeed most of $N_{++} + N_{--}$ has an accidental rather than a physics origin.

We can also use the same-sign events to estimate nonaccidental backgrounds. If the two-particle correlations (R) of the parent hadrons are independent of particle type and satisfy $R_{+-} = (R_{++}R_{--})^{1/2}$, then formula (22) given for accidentals also holds for correlated pairs. The above premise has been shown to be true at the 50% level for ordinary hadrons.²¹ Thus since $N_{++} + N_{--}$ is mostly accidental, we conclude that the same-sign pairs give a good estimate of our backgrounds due to accidentals and decays of ordinary hadrons.

The equal correlation premise is not, however, necessarily true for charmed particles. While reasonable models of charm production do not predict a significant background, not enough is known about charm production (particularly at high p_T) to rule it out.

A final possible source of background at high mass is mismeasured real muon pairs of lower mass. These were effectively eliminated by re-measurement of the muon momentum using the steel magnet.

Figure 10(a) shows our mass spectrum for unlike- and like-sign pairs from data set I at 400 GeV. We see that background is less than 10% for $M_{\mu^+\mu^-} \geq 5$ GeV and drops rapidly at higher masses. We handle this small background by subtracting the spectrum of same-sign pairs from that of opposite-sign pairs. Since, however, the p_T acceptance of same-sign pairs is broader than that of opposite-sign pairs, some care must be taken in order not to bias the p_T distribution at the lowest masses. We therefore use a technique to correct for the difference in same-sign versus opposite-sign p_T acceptance.³⁶ Before calculating the p_T , rapidity, and mass of a same-sign pair, we reflect one of the muons through the horizontal mid-plane of the apparatus. In general this changes

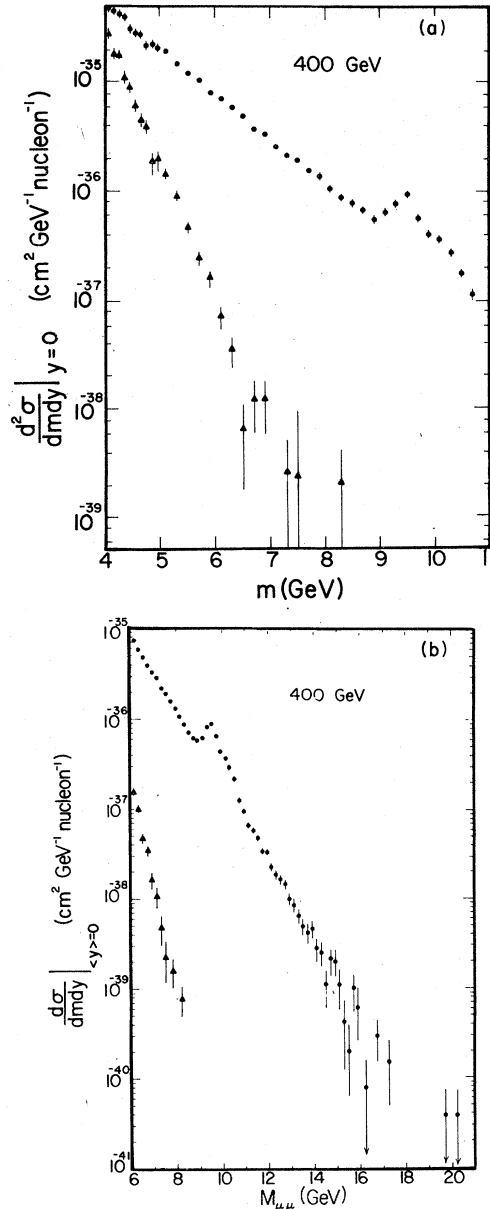


FIG. 10. (a) Dimuon yield for data set I, 400 GeV protons incident. The like-sign pairs are a measure of the contributions from accidentals and pion decay. (b) Dimuon yield for data set III, 400 GeV protons incident. The cross sections in (a) and (b) do not have nucleon motion or radiative corrections. Symbols $\bullet = \mu^+\mu^-$, $\blacktriangle = \mu^+\mu^+ + \mu^-\mu^-$.

the mass and p_T of the pair, but if it is an accidental the reflected pair has the same production cross section as the original pair, and if it is from correlated hadron pair decay the cross sections are approximately the same.

IV. RESULTS

A. Data presentation

Figure 11 shows the differential cross sections $d^2\sigma/dm dy|_{(y)}$ for data sets I and II.³⁷ The overall systematic normalization uncertainty of all the data can be assumed to be less than $\pm 25\%$. Figure 10(b) shows the highest-mass $\mu^+\mu^-$ pair data (data set III, 400 GeV high intensity).

Invariant cross sections versus p_T at 400 GeV are presented in Table XI and shown in Fig. 12. In Fig. 13 we give the moments $\langle p_T \rangle$ and $\langle p_T^2 \rangle$ vs mass. In all cases the moments were calculated directly from the data. The variation of the cross section vs y for various mass bins at three different incident proton energies is shown in Fig. 14(a) and presented in Table XII. We use the scaling form $s d^2\sigma/d\sqrt{\tau} dy$ for convenience. Figure 14(b) shows the slope, at $y=0$, of the distribution shown in Fig. 14(a). The slope will be discussed in detail in Sec. IV D.

B. Scaling

The Drell-Yan model Eq. (4) embodies scaling and we have already published a scaling comparison⁵ in some detail. The exponential scaling fit³⁷

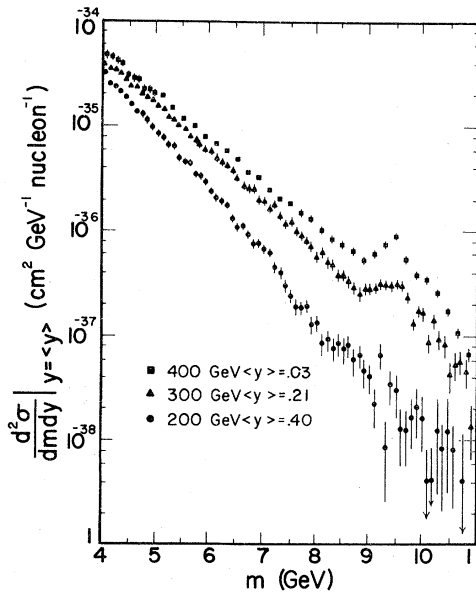


FIG. 11. Yield of dimuon pairs versus mass for incident-proton energies of 200, 300, and 400 GeV. Like-sign pairs were subtracted to correct for accidentals and hadron decays. The cross section per standard nucleon (60% neutron, 40% proton) is defined in the text. The cross sections do not have nucleon-motion or radiative corrections.

to the data is

$$s \left. \frac{d^2\sigma}{d\sqrt{\tau} dy} \right|_{y=0,2} = (42 \pm 0.2 \pm 11.0) \times \exp[-(25.1 \pm 0.1 \pm 0.6)\sqrt{\tau}] \times \mu b \text{ GeV}^2. \quad (24)$$

The scaling data and the fit are shown in Fig. 15. Also shown is a Drell-Yan-model fit which is discussed in detail in Sec. IV C. In Fig. 16, we compare the exponential fit and the Drell-Yan-model fit to our data with preliminary pp data from the CERN ISR.³⁸ We note that the CERN data is all at lower values of $\sqrt{\tau} = x$ and that the higher- s data agrees with the extrapolation of our data within the statistical errors.

It remains to discuss the question whether or not the agreement with scaling is too good, in view of the scaling violations observed in deeply inelastic μN scattering^{10,40} and in neutrino charged-current interactions.⁴¹⁻⁴³

In Fig. 17(a) we present the scaling plot as computed using the QCD calculation of Owens and Reya.⁴⁴ It is seen that in the region $\sqrt{\tau} = 0.15$ to 0.45, the predicted QCD scale-breaking effects are small. The data has insufficient statistics to

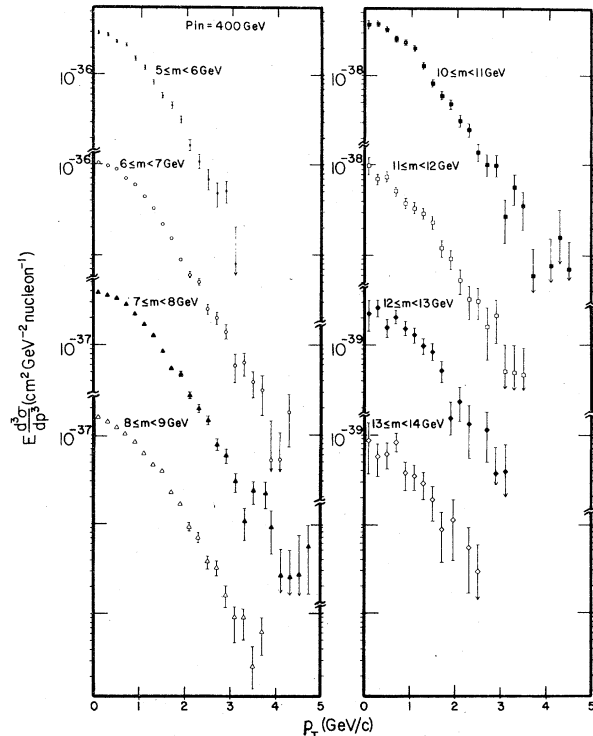


FIG. 12. Invariant yield of dimuons as a function of the transverse momentum p_T of the muon pair for 400 GeV incident protons.

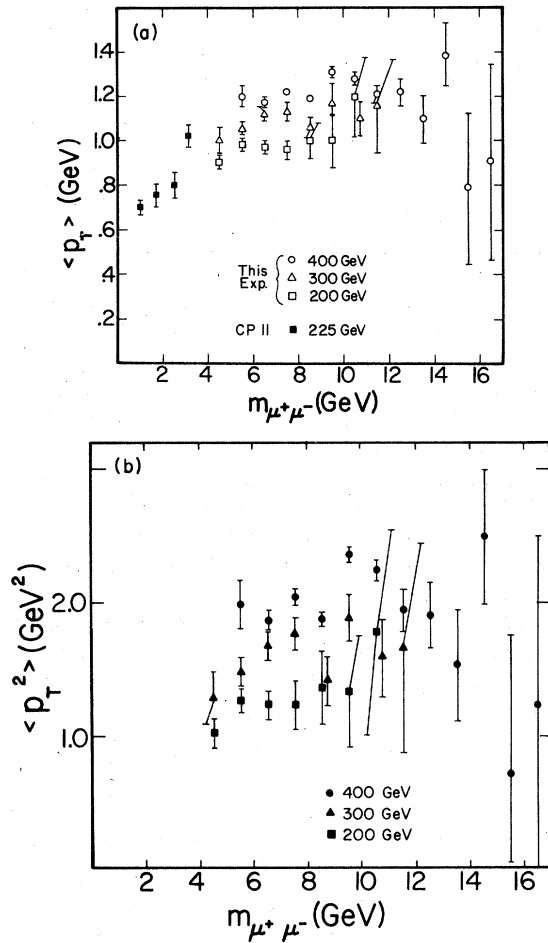


FIG. 13. The average value of $\langle p_T \rangle$ and $\langle p_T^2 \rangle$ for the observed dimuon pairs. Also shown is the data from another Fermilab experiment (Ref. 39).

see such a small variation. The most dramatic evidence for QCD effects is seen in the p_T behavior discussed in Sec. IV E.

C. Extraction of nucleon sea

Equation (4) can be differentiated with respect to rapidity to give the form

$$s \frac{d^2\sigma}{d\sqrt{\tau} dy} = \frac{8\pi\alpha^2}{9\tau^{3/2}} \sum_{u,d,s} e_i^2 [f_i^b(x_b, m^2) \bar{f}_i^t(x_t, m^2) + \bar{f}_i^b(x_b, m^2) f_i^t(x_t, m^2)]. \quad (25)$$

Here we follow the usual procedure of neglecting the heavier (c, b, \dots) quarks. The f 's are the quark structure functions which can be expressed as

$$f_u(x, m^2) \equiv u_v(x, m^2) + u_s(x, m^2). \quad (26)$$

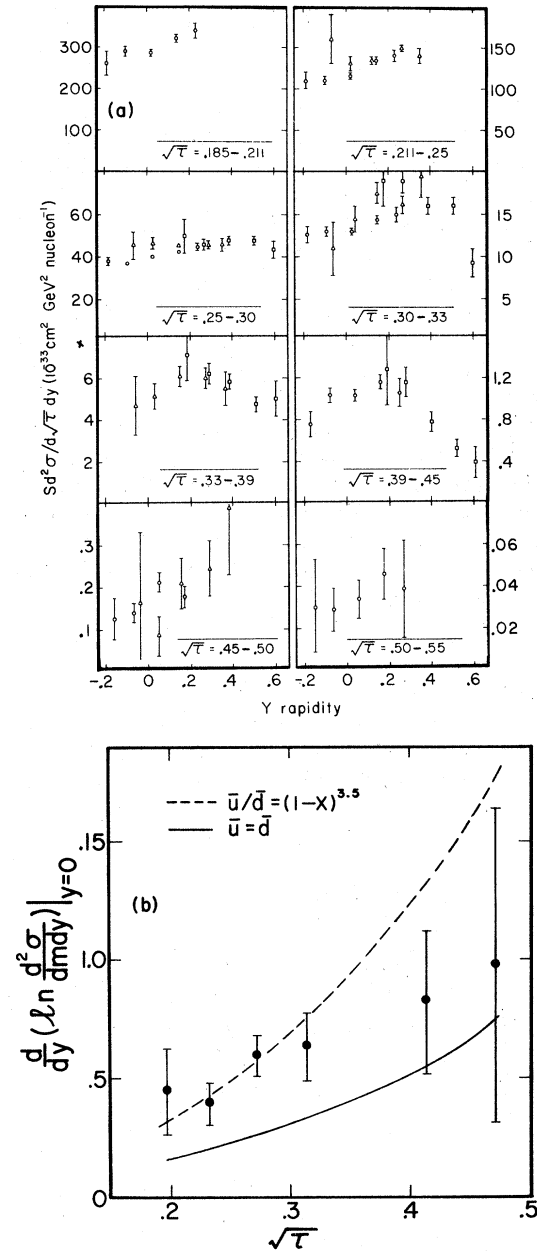


FIG. 14. (a) Yield of dimuons versus the center-of-mass rapidity y , of the pair of muons. $\circ \equiv 400$ GeV, $\triangle \equiv 300$ GeV, and $\square \equiv 200$ GeV. (b) Slope of the rapidity distribution evaluated at $y=0$. The solid line is the Drell-Yan model fit to the data with $\bar{u} = \bar{d}$ and the dashed line is the fit with $\bar{u} \neq \bar{d}$.

taking explicit notice of the fact that the u quark in the proton, for example, has a large component which is due to the presence of u valence quarks and a small piece which comes from the sea of $u\bar{u}$ quark pairs. The f 's are defined such that

$$\int_0^1 f_i(x) dx$$

TABLE XI. Cross section versus rapidity (y) for bins of $\sqrt{\tau} = m/\sqrt{s}$. Nucleon-motion and radiative corrections have been applied to the cross sections as described in the text.

$\sqrt{\tau}$	y	$s \frac{d^2\sigma}{d\sqrt{\tau} dy} (\text{cm}^2 \text{ GeV}^2 \text{ nucleon}^{-1})$		
		400 GeV	300 GeV	200 GeV
0.198	-0.189	$2.59 \pm 0.28 \times 10^{-31}$		
	-0.099	2.88 ± 0.11		
	0.021	2.86 ± 0.08		
	0.141	3.20 ± 0.08		
	0.231	3.37 ± 0.17		
0.229	-0.187	$1.11 \pm 0.10 \times 10^{-31}$		
	-0.097	1.10 ± 0.04		
	-0.067		$1.61 \pm 0.29 \times 10^{-31}$	
	0.023	1.16 ± 0.03	1.29 ± 0.08	
	0.143	1.33 ± 0.04	1.33 ± 0.05	
	0.233	1.40 ± 0.07		
	0.263		1.48 ± 0.06	
	0.353		1.38 ± 0.09	
0.273	-0.184	$3.61 \pm 0.16 \times 10^{-32}$		
	-0.094	3.63 ± 0.07		
	-0.064		$4.55 \pm 0.64 \times 10^{-32}$	
	0.026	3.98 ± 0.05	4.66 ± 0.26	
	0.146	4.25 ± 0.06	4.54 ± 0.17	
	0.176			$5.05 \pm 0.74 \times 10^{-32}$
	0.236	4.45 ± 0.13		
	0.266		4.64 ± 0.17	4.58 ± 0.26
	0.356		4.60 ± 0.32	
	0.386			5.02 ± 0.21
	0.506			5.02 ± 0.21
	0.596			4.35 ± 0.43
0.315	-0.180	$1.27 \pm 0.09 \times 10^{-32}$		
	-0.090	1.27 ± 0.04		
	-0.060		$1.11 \pm 0.32 \times 10^{-32}$	
	0.030	1.33 ± 0.03	1.46 ± 0.15	
	0.150	1.46 ± 0.04	1.76 ± 0.12	
	0.180			$1.89 \pm 0.30 \times 10^{-32}$
	0.240	1.51 ± 0.08		
	0.270		1.63 ± 0.11	1.91 ± 0.04
	0.360		1.94 ± 0.23	
	0.390			1.60 ± 0.09
	0.510			1.60 ± 0.10
	0.600			0.92 ± 0.16
	0.357	-0.057		$4.72 \pm 1.44 \times 10^{-33}$
0.033			5.14 ± 0.59	
0.153			6.07 ± 0.46	
0.183				$7.12 \pm 1.19 \times 10^{-33}$
0.273			6.01 ± 0.49	6.20 ± 0.49
0.363			5.48 ± 0.81	
0.393				5.83 ± 0.36
0.513				4.74 ± 0.35
0.603				4.99 ± 0.85

TABLE XI. (Continued.)

$\sqrt{\tau}$	y	$s \frac{d^2\sigma}{d\sqrt{\tau} dy} (\text{cm}^2 \text{ GeV}^2 \text{ nucleon}^{-1})$		
		400 GeV	300 GeV	200 GeV
0.414	-0.170	$0.70 \pm 0.10 \times 10^{-32}$		
	-0.080	1.00 ± 0.06		
	0.040	1.01 ± 0.05		
	0.160	1.13 ± 0.06		
	0.190			$1.29 \pm 0.35 \times 10^{-33}$
	0.250	0.96 ± 0.12		
	0.280			1.16 ± 0.14
	0.400			0.78 ± 0.09
	0.520			0.53 ± 0.08
	0.610			0.39 ± 0.15
0.473	-0.163	$1.28 \pm 0.47 \times 10^{-34}$		
	-0.073	1.33 ± 0.20		
	-0.043		$1.66 \pm 1.67 \times 10^{-34}$	
	0.047	2.12 ± 0.21	0.87 ± 0.50	
	0.167	1.85 ± 0.23	2.11 ± 0.59	
	0.257	1.82 ± 0.49		
	0.287		2.47 ± 0.67	
	0.377		3.90 ± 1.61	
	0.522			
0.522	-0.157	$3.08 \pm 2.19 \times 10^{-35}$		
	-0.067	2.87 ± 1.00		
	0.053	3.42 ± 0.90		
	0.173	4.57 ± 1.19		
	0.263	3.93 ± 2.28		

is the fraction of the proton's momentum carried by the quark of flavor i . We assume the SU(2) symmetry

$$u^p(x, m^2) = d^n(x, m^2),$$

$$u^n(x, m^2) = d^p(x, m^2),$$

where $p \equiv$ proton and $n \equiv$ neutron.

In principle, sufficient dilepton data over a large enough domain of y , m^2 could be used to unfold the structure functions. Because our data is concentrated near $y=0$, we cannot perform this unfolding without additional knowledge or assumptions. To proceed further, we substitute data from inelastic lepton scattering for the quark distributions $f_i(x, m^2)$. Inelastic electron or muon scattering measures

$$\nu W_2^p(x, Q^2) = \sum_i e_i^2 [f_i^p(x, Q^2) + \bar{f}_i^p(x, Q^2)]. \quad (27)$$

QCD calculations of the underlying subprocesses contributing to lepton scattering and dimuon production^{11,45} suggest the identification of

$$|Q^2| \leftrightarrow |m^2|.$$

Furthermore, the QCD diagrams of these processes, to order $\alpha_s^2 Q^2$, amount to the use of Q^2 -dependent structure functions. We thus use a Q^2 -

dependent fit to the data⁴⁶ on electron-nucleon and muon-proton scattering to provide νW_2^p . We use a fit⁴⁷ suggested by low- Q^2 SLAC data for νW_2^n .

$$\frac{\nu W_2^n}{\nu W_2^p} = 1.0 - 0.8x. \quad (28a)$$

We parametrize the antiquark distributions,

$$\begin{aligned} \bar{d} &= A(1-x)^N, \\ \bar{u} &= A(1-x)^{N+\beta}, \\ \bar{s} &= (\bar{u} + \bar{d})/4. \end{aligned} \quad (28b)$$

The inequality of \bar{u} and \bar{d} , originally suggested by an argument of Feynman and Field,⁴⁸ has recently been discussed within QCD.⁴⁹ The \bar{s} suppression is suggested by neutrino scattering,^{41,50} but it has a small effect on the predicted dimuon rate and the results of our fits. We assume that these antiquark distributions are independent of Q^2 over the observed x range. A QCD analysis⁴⁴ suggests that this should be true to the level of $\sim 10\%$ for $x > 0.2$ and $10 < Q^2 < 300$ [See Fig. 17(b)].

We use νW_2 measurements as input and use the muon-pair data to fit the parameters A , N , and β . The results are given in Table XIII(a) both for the assumption $\bar{u} = \bar{d}$ and for the case where the value of β is determined by the fit. The data

TABLE XII. Invariant cross section ($E d^2\sigma/dp^3$) evaluated at various values of $\langle y \rangle$ and incident-proton energy, in units of 10^{-38} cm² GeV⁻² nucleon⁻¹, with nucleon-motion and radiative corrections applied to the cross section as described in the text.

p_T (GeV)	Mass (GeV)	(a) 400 GeV, $\langle y \rangle = 0.03$									
		5-6	6-7	7-8	8-9	9-10	10-11	11-12	12-13	13-14	
0.0-0.2	2880 ± 120	1040 ± 30	382 ± 16	158 ± 9	117 ± 8	36.5 ± 4.2	9.93 ± 2.14	2.25 ± 0.85	0.87 ± 0.51		
0.2-0.4	2760 ± 80	966 ± 18	354 ± 9	138 ± 5	119 ± 5	37.8 ± 2.5	6.99 ± 0.97	2.59 ± 0.54	0.57 ± 0.23		
0.4-0.6	2300 ± 70	894 ± 16	328 ± 8	122 ± 4	109 ± 4	32.3 ± 1.9	7.53 ± 0.86	1.57 ± 0.35	0.62 ± 0.20		
0.6-0.8	2080 ± 70	707 ± 14	280 ± 7	112 ± 4	94 ± 3	25.7 ± 1.6	5.09 ± 0.60	2.07 ± 0.34	0.85 ± 0.21		
0.8-1.0	1480 ± 60	594 ± 14	221 ± 7	83 ± 3	78 ± 3	23.2 ± 1.4	3.77 ± 0.47	1.54 ± 0.27	0.38 ± 0.13		
1.0-1.2	1180 ± 60	440 ± 12	170 ± 6	63 ± 3	50 ± 2	19.9 ± 1.3	3.34 ± 0.43	1.29 ± 0.24	0.35 ± 0.11		
1.2-1.4	817 ± 48	330 ± 11	125 ± 5	47 ± 2	44 ± 2	12.8 ± 1.0	2.89 ± 0.40	0.97 ± 0.20	0.29 ± 0.10		
1.4-1.6	590 ± 43	217 ± 9	86 ± 4	39 ± 2	33 ± 2	8.2 ± 0.8	2.31 ± 0.37	0.85 ± 0.18	0.19 ± 0.08		
1.6-1.8	458 ± 37	153 ± 7	55 ± 3	23 ± 2	23 ± 2	6.0 ± 0.6	1.20 ± 0.25	0.52 ± 0.14	0.09 ± 0.05		
1.8-2.0	319 ± 32	88 ± 6	47 ± 3	17.1 ± 1.2	15.1 ± 1.2	4.8 ± 0.6	0.91 ± 0.22	0.16 ± 0.08	0.11 ± 0.07		
2.0-2.2	167 ± 24	61 ± 5	27 ± 2	9.5 ± 1.1	12.2 ± 1.1	3.2 ± 0.5	0.52 ± 0.16	0.24 ± 0.10			
2.2-2.4	111 ± 21	50 ± 4	20 ± 2	7.2 ± 0.9	7.8 ± 0.9	2.5 ± 0.4	0.32 ± 0.13	0.13 ± 0.08	0.057 ± 0.041		
2.4-2.6	71 ± 19	25 ± 3	14 ± 2	3.9 ± 0.7	5.6 ± 0.7	1.4 ± 0.3	0.31 ± 0.12		0.030 ± 0.030		
2.6-2.8	49 ± 15	20 ± 3	7.7 ± 1.2	3.3 ± 0.6	4.4 ± 0.6	1.0 ± 0.3	0.16 ± 0.10	0.12 ± 0.07			
2.8-3.0	53 ± 14	14 ± 3	5.8 ± 1.1	1.6 ± 0.4	2.9 ± 0.5	1.0 ± 0.3	0.21 ± 0.11	0.037 ± 0.037			
3.0-3.2	8 ± 13	5.9 ± 2.1	3.0 ± 0.7	0.84 ± 0.36	1.55 ± 0.36	0.28 ± 0.14	0.050 ± 0.050	0.039 ± 0.039			
3.2-3.4		6.4 ± 1.9	1.1 ± 0.4	0.83 ± 0.32	1.38 ± 0.36	0.58 ± 0.22	0.049 ± 0.049				
3.4-3.6	26 ± 13	3.8 ± 1.2	2.4 ± 0.7	0.26 ± 0.18	1.05 ± 0.32	0.35 ± 0.16	0.046 ± 0.046				
3.6-3.8	10 ± 10	3.1 ± 1.5	2.2 ± 0.7	0.63 ± 0.7	0.71 ± 0.25	0.06 ± 0.06					
3.8-4.0		0.5 ± 0.9	0.94 ± 0.47		0.44 ± 0.20						
4.0-4.2		0.5 ± 0.5	0.26 ± 0.27		0.51 ± 0.21	0.08 ± 0.08					
4.2-4.4		1.8 ± 1.0	0.26 ± 0.26		0.21 ± 0.15	0.16 ± 0.16					
4.4-4.6	27 ± 28	-1.5 ± 1.5	0.28 ± 0.48		0.38 ± 0.19	0.07 ± 0.07					
4.6-4.8			0.57 ± 0.40	0.15 ± 0.15							
4.8-5.0		1.2 ± 1.2									

TABLE XII. (Continued.)

p_T (GeV)	Mass (GeV)	(b) 300 GeV, $\langle y \rangle = 0.21$									
		4-5	5-6	6-7	7-8	8-9	9-10	10-11	11-12		
0.0-0.2	9160 ± 420	2570 ± 160	849 ± 70	286 ± 39	96 ± 20	91 ± 21	18.7 ± 7.2	2.71 ± 2.72			
0.2-0.4	7650 ± 300	2300 ± 100	783 ± 43	253 ± 22	70 ± 11	66 ± 10	16.6 ± 4.0	0.79 ± 0.79			
0.4-0.6	6610 ± 300	2070 ± 100	655 ± 35	237 ± 19	70 ± 9	66 ± 8	12.1 ± 2.6	1.01 ± 0.72			
0.6-0.8	5580 ± 300	1820 ± 110	540 ± 33	197 ± 16	73 ± 9	69 ± 9	10.1 ± 2.2	1.00 ± 0.58			
1.8-1.0	3910 ± 270	1130 ± 80	414 ± 30	145 ± 14	53 ± 7	50 ± 7	62.4 ± 1.6	0.68 ± 0.48			
1.0-1.2	2730 ± 230	872 ± 73	286 ± 24	110 ± 12	52 ± 8	50 ± 7.7	6.6 ± 1.7	1.18 ± 0.60			
1.2-1.4	1850 ± 200	635 ± 61	187 ± 19	78.1 ± 9.8	32 ± 6	30 ± 5.6	2.3 ± 0.9	0.26 ± 0.26			
1.4-1.6	1580 ± 200	384 ± 42	182 ± 20	38.0 ± 7.2	18 ± 4	16.6 ± 4.0	3.7 ± 1.2	0.54 ± 0.38			
1.6-1.8	838 ± 155	260 ± 38	110 ± 14	46.4 ± 8.2	10.2 ± 3.4	9.7 ± 3.3	4.6 ± 1.4	0.35 ± 0.35			
1.8-2.0	503 ± 136	124 ± 25	72 ± 13	19.2 ± 4.9	2.3 ± 1.3	2.2 ± 1.3	0.75 ± 0.53				
2.0-2.2	397 ± 102	103 ± 22	40.8 ± 9.9	25.0 ± 6.0	7.0 ± 3.0	6.7 ± 2.9	0.47 ± 0.47	0.29 ± 0.30			
2.2-2.4	189 ± 84	79 ± 23	21.9 ± 6.8	11.8 ± 4.1	1.6 ± 1.2	1.55 ± 1.12					
2.4-2.6	58 ± 101	32 ± 13	19.0 ± 6.5	5.2 ± 2.7	0.88 ± 0.89	0.84 ± 0.84					
2.6-2.8	212 ± 194	14 ± 12	7.9 ± 4.0				0.37 ± 0.37				
2.8-3.0	-139 ± 108	6.6 ± 11.5	11.0 ± 5.0	1.1 ± 1.1			0.44 ± 0.44				
3.0-3.2		5.5 ± 9.6	1.9 ± 1.9	1.2 ± 1.2	1.0 ± 1.0	0.96 ± 0.98					
3.2-3.4			2.3 ± 2.3								
3.4-3.6											
3.6-3.8			2.8 ± 2.9								
3.8-4.0		13.3 ± 13.8									
4.0-4.2			1.7 ± 1.7								
4.2-4.4											
4.4-4.6			1.7 ± 1.7								

TABLE XII. (Continued.)

\hat{p}_T (GeV)	Mass (GeV)	(c) 200 GeV, $\langle y \rangle = 0.40$									
		4-5	5-6	6-7	7-8	8-9	9-10	10-11			
0.0-0.2	6290 ± 320	1630 ± 110	399 ± 43	94.5 ± 18.8	22.2 ± 7.5	15.8 ± 6.1	2.09 ± 2.12				
0.2-0.4	5880 ± 240	1440 ± 80	342 ± 25	90.1 ± 11.1	16.5 ± 3.8	1.86 ± 1.08	1.23 ± 0.88				
0.4-0.6	4750 ± 230	1190 ± 70	333 ± 22	70.2 ± 8.4	13.4 ± 2.9	4.28 ± 1.45	0.42 ± 0.42				
0.6-0.8	3690 ± 220	1040 ± 70	255 ± 20	52.2 ± 6.9	10.0 ± 2.3	2.27 ± 0.94	0.32 ± 0.33				
0.8-1.0	2930 ± 220	601 ± 51	181 ± 17	41.1 ± 6.1	6.1 ± 1.7	4.37 ± 1.35	0.26 ± 0.27				
1.0-1.2	1680 ± 160	441 ± 43	130 ± 14	29.7 ± 5.4	5.2 ± 1.6	1.22 ± 0.62	0.71 ± 0.42				
1.2-1.4	1260 ± 140	248 ± 30	73 ± 11	16.4 ± 3.8	6.0 ± 1.8	2.20 ± 0.92	0.31 ± 0.31				
1.4-1.6	678 ± 124	255 ± 36	45 ± 8	9.5 ± 2.9	1.7 ± 1.0	0.35 ± 0.35	0.36 ± 0.36				
1.6-1.8	598 ± 102	159 ± 28	35 ± 7	6.9 ± 2.5	1.05 ± 0.75						
1.8-2.0	59 ± 67	63 ± 15	20 ± 6	3.7 ± 1.7	1.05 ± 0.75	0.37 ± 0.37	0.61 ± 0.46				
2.0-2.2	176 ± 62	44 ± 16	8.3 ± 3.7	3.2 ± 1.9	0.58 ± 0.58	0.42 ± 0.43					
2.2-2.4	-33 ± 55	50 ± 16	9.4 ± 4.3	1.6 ± 1.2		0.38 ± 0.39					
2.4-2.6	105 ± 56	8.1 ± 8.3	5.3 ± 3.1								
2.6-2.8	-73 ± 75	11.8 ± 8.7	1.8 ± 1.8								
2.8-3.0		4.2 ± 4.2									
3.0-3.2				1.1 ± 1.2							
3.2-3.4					0.53 ± 0.53						

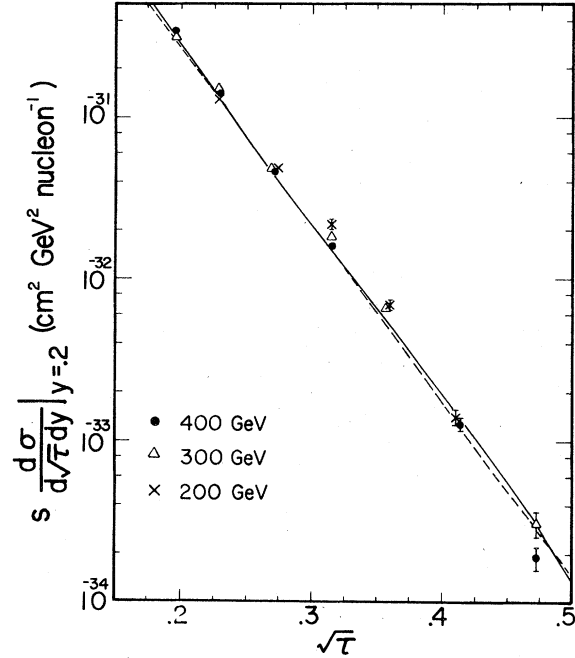


FIG. 15. Scaling form of the cross section for 200, 300, and 400 GeV data with the exponential scaling fit defined in text. The dotted line is the exponential fit described in the text. The solid line is the Drell-Yan-model fit to the data for \bar{u} and \bar{d} .

clearly favor $\bar{u} \neq \bar{d}$.

For the results in Table XIII(a) we assumed no Q^2 dependence in Eq. (28a). The QCD calculation of Owens and Reya⁴⁴ can be used to obtain an estimate for the expected Q^2 dependence of the ratio. Using the data of Bodek *et al.*⁴⁷ in the range $0.2 \leq x \leq 0.6$ and correcting the data to m^2 appropriate for our 300 GeV data we obtain

$$\frac{\nu W_2^n}{\nu W_2^p} = 0.807 - 0.535x. \quad (28c)$$

The result of the fit using Eq. (28c) is shown in Table XIII(b). The data still favor $\bar{u} \neq \bar{d}$.

We can avoid parametrizing the antiquark distributions and extract them directly if we assume a relationship between the flavors of antiquark, e.g., the floating fit of Table XIII(a):

$$\bar{u}(x)/\bar{d}(x) = (1-x)^{3.48},$$

$$s(x) = \bar{s}(x) = (\bar{u}(x) + \bar{d}(x))/4.$$

To do this we take data pairs at symmetric y values, the νW_2^p measurements, and Eq. (28a) for νW_2^n at the corresponding $x_b = \text{beam}$ and $x_t = \text{target}$. We then have a system of six unknowns and six measurements:

$$u(x_b), u(x_t), d(x_b), d(x_t), \bar{d}(x_b), \bar{d}(x_t);$$

$$\frac{s d^2\sigma}{d\sqrt{\tau} dy} (+y, \sqrt{\tau}, m^2), \frac{s d^2\sigma}{d\sqrt{\tau} dy} (-y, \sqrt{\tau}, m^2),$$

$$\nu W_2^p(x_b, m^2), \nu W_2^p(x_t, m^2),$$

$$\nu W_2^n(x_b, m^2), \nu W_2^n(x_t, m^2).$$

Most of the 400-GeV data and one third of the 300-GeV data provide us with suitable data pairs.

Figure 18(a) shows the results for $\bar{u} + \bar{d}$, the sea combination most independent of our assumptions about relative antiquark strengths. It is also possible to form the quantity $\bar{q}(x) + \bar{s}(x) \equiv \bar{u}(x) + \bar{d}(x) + 2\bar{s}(x)$. In Fig. 18(b) we compare our values of $\bar{q}(x) + \bar{s}(x)$ to those measured in inelastic neutrino scattering at CERN⁴¹ and at Fermilab.⁴³

The comparison involves the explicit factor of 3 for color in dilepton production and also the QCD prediction that $Q^2 \rightarrow m^2$. Our values of $\bar{q}(x) + \bar{s}(x)$ appear to lie about 70% higher than the neutrino data in the vicinity of $\sqrt{\tau} = 0.2$. Note, however, that for the same $\sqrt{\tau}$ the average Q^2 for the neutrino data is lower than that for the dilepton data;

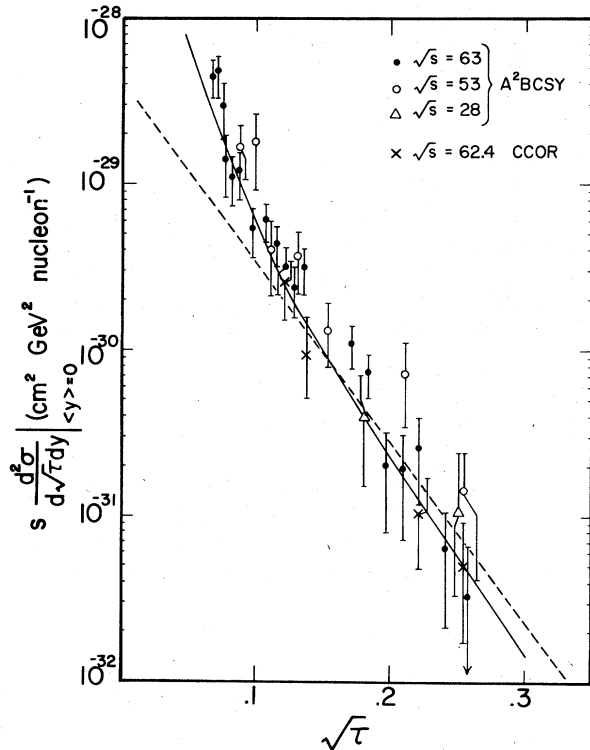


FIG. 16. CERN ISR (Ref. 38) dilepton data. The dotted line is the exponential fit defined in the text and the solid line is a Drell-Yan-model fit to this experiment's dimuon data, taking into account the fact that the CERN data are proton on proton and our data is proton on nucleon.

a correction computed using the results of Owens and Reya⁴⁴ [Fig. 17(b)] would slightly lower the neutrino points at $\sqrt{\tau} = 0.2$, increasing the discrepancy.

We therefore observe a dilepton production rate larger than would be predicted by the Drell-Yan model using the $F_2(x, Q^2)$ from muon scattering and $\bar{q}(x)$ from neutrino data. Recent results from experiments at the CERN SPS indicate that dimuon production for π -nucleon collisions is larger than the Drell-Yan calculation by approximately a factor of 2.⁵¹ This discrepancy was not observed in an earlier measurement made at Fermilab.⁵²

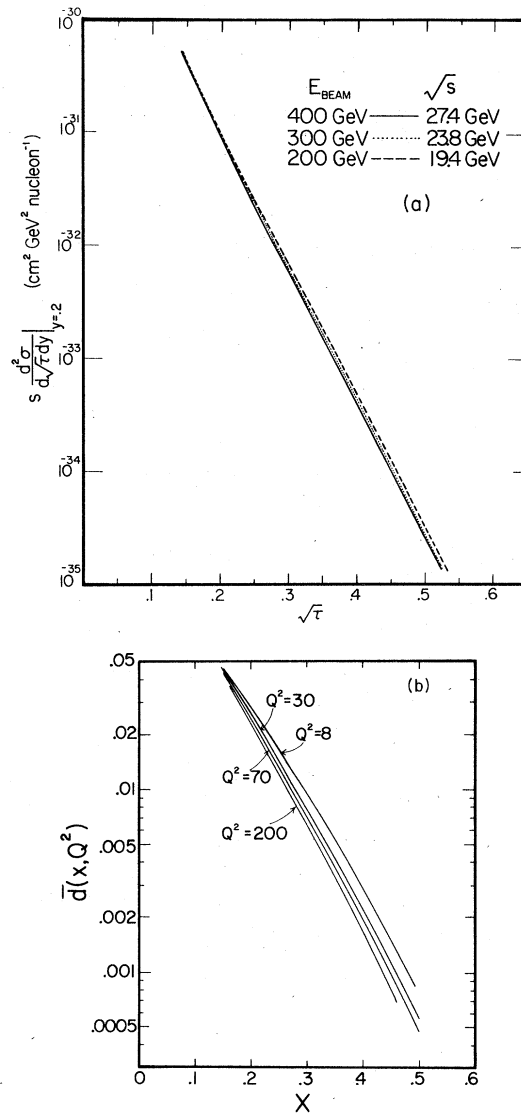


FIG. 17. (a) Cross section vs $\sqrt{\tau}$ at three different beam energies, computed following a QCD calculation by Owens and Reya (Ref. 44). (b) Sea distribution using the QCD calculation by Owens and Reya.

Several recent calculations of QCD contributions of next order (beyond leading logarithm) for both deep-inelastic scattering and dilepton production have the effect of increasing the theoretical dilepton yields by about a factor of 2.^{53, 54} This factor is independent of x for $x < 0.5$. However, lacking calculations or estimates of contributions from yet higher orders, the consistency of experiment and theory must be taken as somewhat fortuitous. Taking a broader view, agreement of the dilepton data with the neutrino-scattering data within a factor of 2 represents a substantial success for the quark-parton model.

D. Slope at zero rapidity

The difference in the \bar{u} and \bar{d} content of a proton, which was considered in the previous section, also manifests itself in the slope of the data in Fig. 14(a) near $y = 0$. We assume that the higher-order corrections mentioned in Sec. IVC are not y dependent. The doubly differential cross section

$$s \frac{d^2\sigma}{d\sqrt{\tau} dy}$$

must be symmetric relative to $y = 0$ for pp collisions. However, the quark-parton model favors a positive slope in y for pn collisions and therefore also p -Cu collisions since the "nucleon" in Cu is 40% proton and 60% neutron. This slope near $y = 0$ is the result of several features of the model; first, the larger number of charge $\frac{2}{3}$ u quarks in

TABLE XIII. Parameters for nucleon-sea fit, $\bar{d} = A(1-x)^N$, $\bar{u} = A(1-x)^{N+\beta}$, $\bar{s} = (\bar{u} + \bar{d})/4$. The first error is statistical and the second when given is systematic.

(a) No Q^2 dependence	
A. Fix $\bar{u} = \bar{d}$	
	$A = 0.476 \pm 0.011$
	$N = 8.62 \pm 0.08$
	$\chi^2/DF = 300/154$
B. Allow β to float	
	$A = 0.548 \pm 0.002 \pm 0.17$
	$\beta = 3.48 \pm 0.25 \pm 1.2$
	$N = 7.62 \pm 0.08 \pm 0.38$
	$\chi^2/DF = 211/156$
(b) Using Q^2 correction for νW_2^{η}	
A. Fix $\bar{u} = \bar{d}$	
	$A = 0.504 \pm 0.011$
	$N = 8.69 \pm 0.08$
	$\chi^2/DF = 249/154$
B. Allow β to float	
	$A = 0.536 \pm 0.016$
	$\beta = 2.51 \pm 0.39$
	$N = 7.77 \pm 0.11$
	$\chi^2/DF = 208/155$

the proton, second, the increase of u/d as $x \rightarrow 1$ observed in electron scattering, and third, the possible SU(3)-violating dominance of \bar{d} over \bar{u} quarks in the proton

$$\bar{u}(x) - \bar{d}(x) < 0, \quad (29)$$

which is mirrored as a dominance of the \bar{u} sea in the neutron. It is interesting that this same quantity appears in the QPM interpretation of the Adler

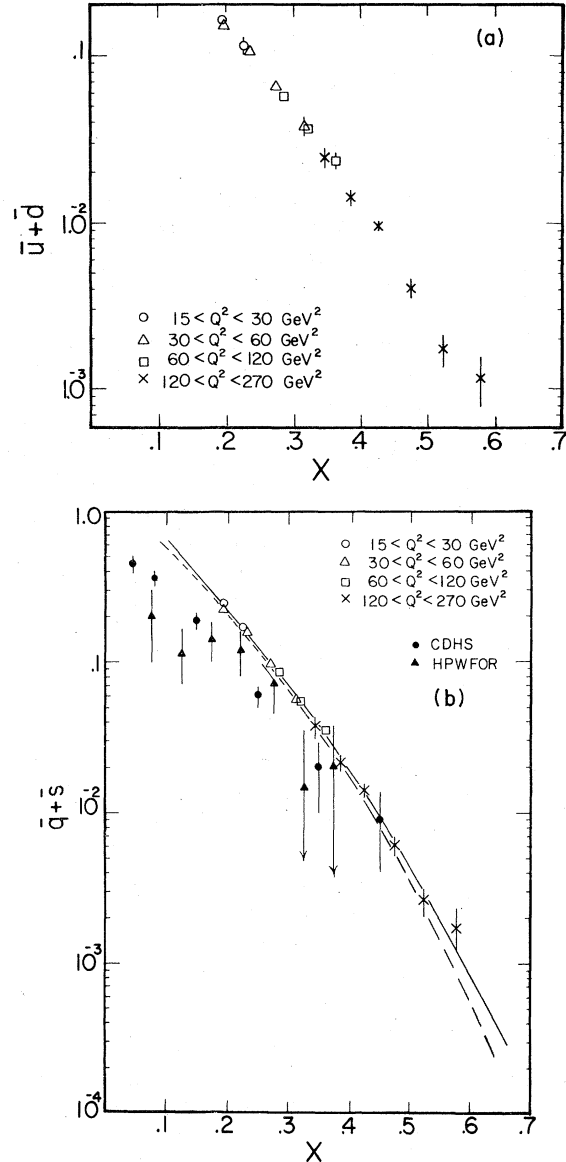


FIG. 18. $\bar{u} + \bar{d}$ distribution for this experiment for various Q^2 bins. (b) Sea distribution for this experiment for various Q^2 bins. Also shown are data points from CERN-Dortmund-Heidelberg-Saclay (Ref. 41) and Harvard-Pennsylvania-Wisconsin-Fermilab-Ohio State-Rutgers (Ref. 43). The dotted line is the fit with $\bar{u} = \bar{d}$ and the solid line is the fit with $\bar{u} = \bar{d}(1-x)$.^{3, 48}

sum rule^{55, 56}

$$\begin{aligned}\Delta &\equiv \int_0^1 (\nu W_2^{ep} - \nu W_2^{en}) \frac{dx}{x} - 0.33 \\ &= \frac{2}{3} \int_0^1 (\bar{u} - \bar{d}) dx.\end{aligned}$$

The negative value of Δ derived from experiment motivated Feynman and Field⁴⁸ to propose the relation

$$\bar{d} = \bar{u}(1-x)^3. \quad (30)$$

Figure 14(b) plots, versus $\sqrt{\tau}$, the slope

$$\frac{d}{dy} \left[\ln \left(s \frac{d^2\sigma}{d\sqrt{\tau} dy} \right) \right]_{y=0} \quad (31)$$

obtained by fitting the data in Fig. 14(a) near $y=0$. The slopes are larger than the Drell-Yan-model fit which assumes asymmetries only in the valence u and d distributions (solid curve). Thus the data favors a surplus of \bar{d} quarks over \bar{u} quarks in the proton. This has been examined recently in QCD theory by Ross and Sachrajda.⁴⁹ They evaluated QCD diagrams which contribute to the structure functions derived in lepton scattering. This enables them to calculate a contribution to Eq. (29) and to show that it is indeed negative but perhaps a factor of 5 smaller than implied by the Adler sum rule. The connection between the Adler difference and Eq. (29) is also discussed by Contouris and Papadopoulos.⁵⁵ We note that whereas the dilepton data establishes the symmetry breaking for $x > 0.2$, the Adler integral is dominated by the small- x region.

E. Transverse momentum of lepton pairs

The simple application of the quark model for dilepton production predicts very small transverse momentum for the dileptons. The observation of average dilepton transverse momentum of the order of 1 GeV and larger provided qualitative support for QCD descriptions of dilepton production. The large $\langle p_T \rangle$ comes about because of the probability (order α_s) of one of the colliding quarks to radiate a hard gluon and recoil to large p_T . Figure 19 shows the experimental results plotted vs $\sqrt{\tau}$ for this experiment, another Fermilab experiment,³⁹ and ISR experiments.³⁸ The increase of average p_T with \sqrt{s} is a direct prediction of QCD.^{14, 17, 57}

We find for $\sqrt{\tau} = 0.21$, using our 300 and 400 GeV data and the ISR³⁸ data,

$$\langle p_T \rangle = (0.028\sqrt{s} + 0.37) \text{ GeV} \quad (32)$$

(\sqrt{s} in GeV) in approximate agreement with the predictions of QCD. Note that the slope is calculable from perturbation theory whereas the intercept

(intrinsic p_T of the quarks) is related to the confining force. Equation (32) is the most dramatic confirmation of QCD (gluon effects) as applied to dilepton production.

F. Explicit QCD contributions

It is of further interest to see if a Drell-Yan calculation including explicit contributions from QCD diagrams involving gluon emission and absorption can be accommodated by the data. Ignoring higher-order corrections, Altarelli *et al.*¹⁷ and Kajantie and Raitio⁵⁷ have presented such calculations. They remove the divergence of the gluon propagator at small momenta by assigning a constant exponential "intrinsic" momentum to the bound-state quarks within a hadron. The fit then involves a time-consuming folding over the intrinsic Fermi momentum k_T , of the quark at each data point. In addition to the parameters A , N , and β introduced above to describe the antiquark distributions, we introduce $g(x) = B(1-x)^n$, the gluon distribution within a nucleon $f(k_T) = e^{-ak_T^2}$, the intrinsic "Fermi motion" of the quarks bound in the nucleon, and α_s , the strong coupling constant at the gluon-quark vertex. We then fit all the data in bins of m , y , and p_T at the three energies 200, 300, and 400 GeV simultaneously. Again we assume no explicit Q^2 dependence of the parameters in the limited range of our fit. The results are

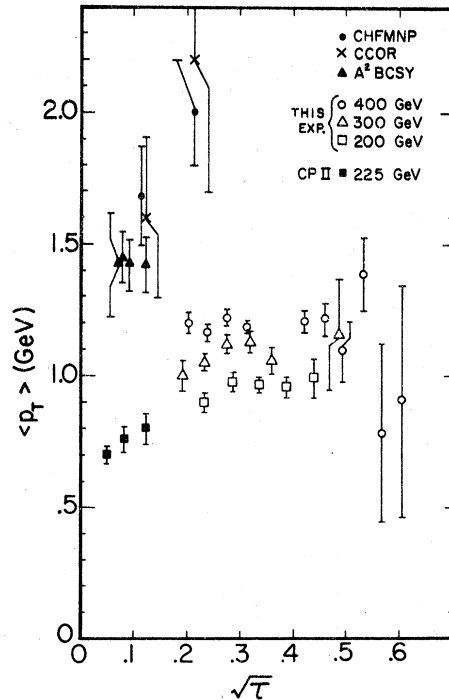


FIG. 19. Average p_T vs $\sqrt{\tau}$ for this experiment compared with Fermilab (Ref. 39) and ISR (Ref. 38) data.

given in Table XIV. Note that the fit is quite good and that the parameters have reasonable values. No detailed study has been made of the error matrix because we believe that systematic errors may well dominate.

G. Muon-electron universality

As a final topic, we present data on muon-electron universality. Figure 20 shows the data obtained on the dielectron continuum. Superimposed in the insert is the muon data. It appears that μe universality holds (to 50% or better) in the production of massive lepton pairs near $\langle Q^2 \rangle \sim 40 \text{ GeV}^2$.

V. CONCLUSIONS

In summary, we find a linear nucleon-number dependence for the dimuon production cross section using Be and Pt targets. The dimuon continuum cross sections scale over the energy and mass range studied by this experiment. In addition, fits to our data using the Drell-Yan model⁸ are in good agreement with the ISR data³⁸ when extrapolated to their range of $\sqrt{\tau}$.

The sea quark distribution as measured by this experiment is about a factor of $1.7_{-0.58}^{+0.73}$ above the sea distribution determined from neutrino experiments. The fits to our data indicate that the \bar{u} distribution in the proton is suppressed relative to the \bar{d} distribution.

We can obtain a good fit simultaneously to the y , p_T , and mass dependence of the dimuon cross section using the model of Altarelli *et al.*¹⁷ and Kajantie *et al.*⁵⁷ The gluon distribution determined by the fit is $g(x) = 2.55(1-x)^{4.1}$ and the value $\alpha_s = 0.27$.

Scaling violations as expected from QCD calculations are observed in the dependence of $\langle p_T \rangle$ with \sqrt{s} at fixed $\sqrt{\tau}$.

TABLE XIV. Explicit QCD fit parameters.

$\bar{d} = A(1-x)^N$
$\bar{u} = A(1-x)^{N+\beta}$
$\bar{s} = (\bar{u} + \bar{d})/4$
$g = B(1-x)^m$
$f = e^{-ak_T^2}$
$A = 0.56 \pm 0.01$
$N = 8.1 \pm 0.1$
$\beta = 2.6 \pm 0.3$
$B = 2.55$ (fixed by $\int g(x) dx = 0.5$)
$m = 4.1 \pm 0.2$
$\alpha_s = 0.27 \pm 0.01$
$a = 1.14 \pm 0.02 \text{ GeV}^{-2}$
$\chi^2/\text{DF} = 805/876$

ACKNOWLEDGMENTS

We would like to express our thanks and appreciation to the many people from Fermilab and the participating institutions who made this experiment possible. In particular, we wish to thank our excellent technicians K. Gray, K. Kephart, F. Pearsall, T. Reagan, and J. Upton as well as the able staff of the Fermilab Proton Department and the Accelerator Division. We would also like to thank M. Luba, M. Bennett, and M. Fisk for the typing of this manuscript and E. Luisada and J. Schellpfeffer for drawing the figures. We are grateful to A. VanGinneken of Fermilab for modifying his hadronic cascade program for our use in the design studies for our target box. We would also like to thank A. Buras for many informative discussions. This work was funded in part by the National Science Foundation and the U. S. Department of Energy.

APPENDIX: THE DATA-ACQUISITION SYSTEM

Figure 21 is a block diagram of the data-acquisition system. The system is very flexible and allowed the trigger requirements to be studied and modified as the data taking progressed.

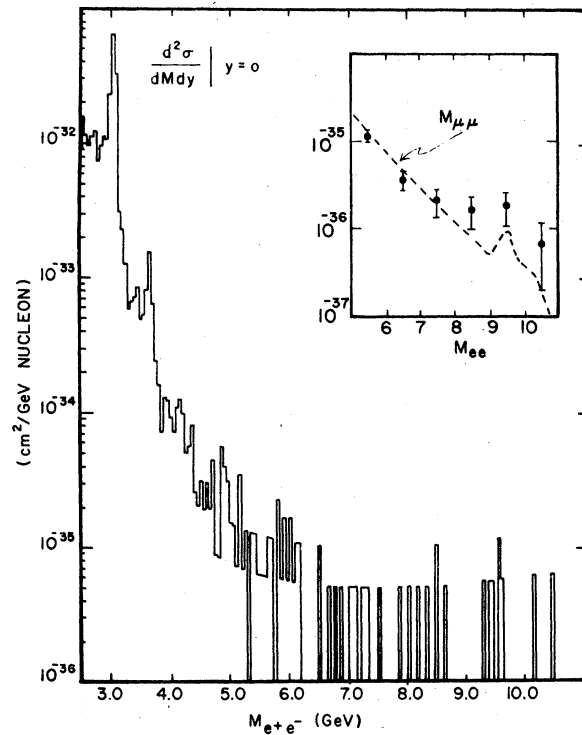


FIG. 20. Dielectron yield for 400-GeV incident protons from a previous CFS experiment. Shown in the inset with wider binning is the dielectron spectrum compared with the dashed line which is a fit to the dimuon data from this experiment.

1. Fast trigger logic

Figure 22 is a diagram of the fast logic. The first-stage triggering decision was made by a LeCroy Model No. 380 multiplicity-logic unit for each arm, set to require four out of five of H1, C, H2, H3, and V4. This crudely defines a track traversing the entire length of the arm. This signal was called T ,

$$T = (H1, C, H2, H3, V4)^4_5.$$

We used a multiplicity trigger rather than a coincidence of all five counters so that events could be recorded in which one of the counters failed to fire, allowing us to monitor the efficiencies of the trigger counters. Typical T rates were 100 kHz; individual trigger counter rates ranged from 0.5 to 5 MHz.

The loose muon-pair trigger was formed from the T signals of both arms by a LeCroy Model No. 364 majority-logic unit (which is capable of 150-MHz operation) set to twofold coincidence:

$$T_{UD} = T_U \cdot T_D,$$

where U refers to one arm and D refers to the other. Also formed was the out-of-time coincidence

$$T_{UDAX} = T_U \cdot T_D(\text{delayed})$$

used to monitor accidental-coincidence rates; T_D (delayed) was delayed by 57 nsec (three accelerator rf buckets) relative to T_U by the insertion of extra cable. The T_{UD} rate was about 1 kHz, the T_{UDAX} rate roughly half that. The T_{UD} rate was dominated by accidental two-arm coincidences. It counted more than T_{UDAX} because the rf buckets did not all contain the same number of protons; occasional buckets containing several times more than the average made the probability of generating a T_{UD}

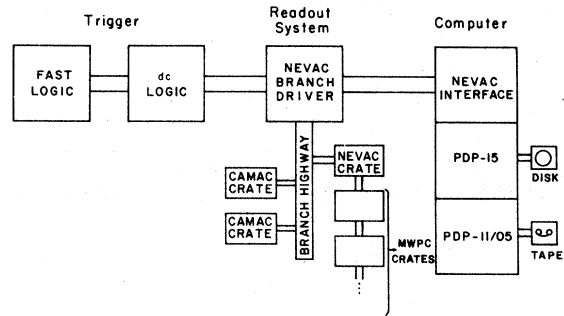


FIG. 21. Data-acquisition system.

higher than the probability of generating a T_{UDAX} . T_{UD} and T_{UDAX} together enabled us to monitor the rf structure of the beam, and T_{UDAX} , together with T_U and T_D , enabled monitoring of beam structure on a slower time scale.

The T_U and T_D signals prescaled by 128 and the T_{UD} signal generated a trigger-fan-in (T_{FI}) gate for the MWPC coincidence registers (CR's) and triggered the dc logic.

2. dc logic

The dc logic (Fig. 23) was a sophisticated and flexible general-purpose triggering system designed by H. Cunitz and W. Sippach at Columbia University's Nevis Laboratories. Input signals were strobed by the T_{FI} signal and latched, so that further processing could be done with dc levels without worrying about timing. Two 16-bit "logic bus" crates containing logic modules had these dc signals bused along their backplanes and available to every module. Each module formed the "and" of any of the 16 bus signals or their complements (selectable by the insertion of pins) as well as an optional input signal from some other module. The

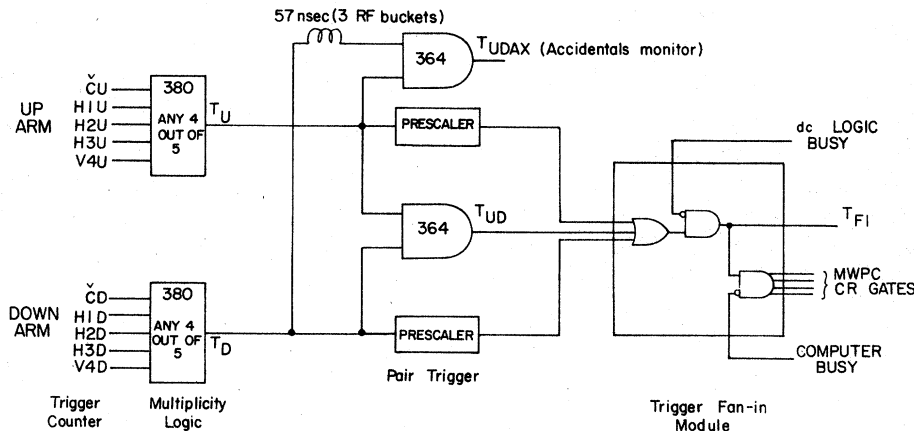


FIG. 22. Fast logic.

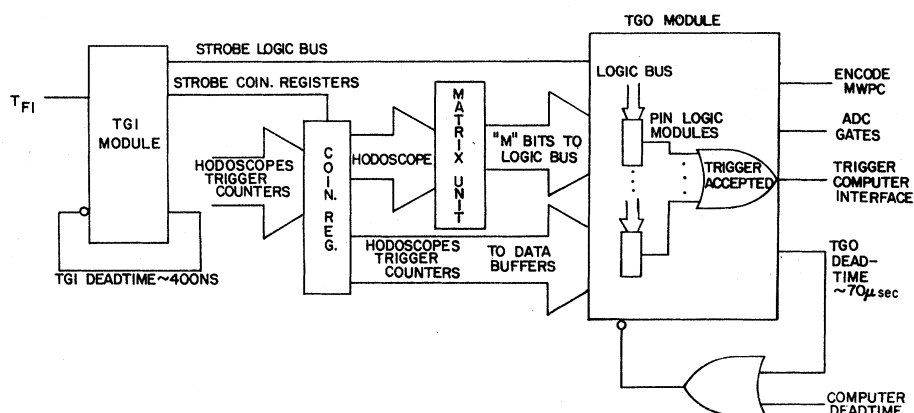


FIG. 23. dc logic.

outputs included a "trigger" signal and complementary logic signals which could be connected to other logic module inputs, as well as an "inhibit" input for prescaling and scaler outputs with and without deadtime. The dc logic could be run with as little as 100 nsec deadtime per T_{FI} , but since our T_{FI} rate was so low we set it to 400 nsec to simplify timing and to cover dead times in the readout system.

The T_{FI} signal from the fast logic came to the trigger generator input (TGI) module which strobed the logic bus and hodoscope CR's and started the dc logic decision cycle. A "matrix unit" for each arm was used to discriminate

against tracks originating upstream of the target in vacuum windows, etc., or downstream in the shielding. It looked for pairs of hodoscope elements of the form (V_1, V_4) which lay near the diagonal of the V_1-V_4 matrix (if no such pair of elements fired the track did not point back to the target) and set a logic bus bit (called M) if one was found.

We used the dc logic to implement one main muon-pair trigger and four study triggers, two pair and two single-arm. The prescaled study triggers required only subsets of the main muon-pair trigger requirements in order to check the efficiency of the various trigger elements.

*Present address: Fermi National Accelerator Laboratory, Batavia, Illinois 60510

†Present address: Nevis Laboratories, Columbia University, Irvington, New York 10533.

‡Present address: Riverside Research, 80 West End Ave., New York, New York 10023.

§Present address: Physics Dept., Gallaudet College, Washington, D.C. 20002.

||Present address: SLAC, P.O. Box 4349, Stanford, California 94305.

¹D. C. Hom *et al.*, Phys. Rev. Lett. **36**, 1236 (1976); H. D. Snyder *et al.*, *ibid.* **36**, 1415 (1976); B. C. Brown *et al.*, Fermilab Report No.-PUB-77/54-EXP, 1977 (unpublished); H. D. Snyder, Ph.D. thesis, Columbia University, 1977 (unpublished); D. C. Hom, Ph.D. thesis, Columbia University, 1977 (unpublished).

²D. C. Hom *et al.*, Phys. Rev. Lett. **37**, 1374 (1976).

³S. W. Herb *et al.*, Phys. Rev. Lett. **39**, 252 (1977); W. R. Innes *et al.*, *ibid.* **39**, 1240 (1977).

⁴D. M. Kaplan *et al.*, Phys. Rev. Lett. **40**, 435 (1977).

⁵J. K. Yoh *et al.*, Phys. Rev. Lett. **41**, 684 (1978).

⁶The most complete description of the dimuon apparatus used to obtain most of the data below is contained in D. M. Kaplan, Ph.D. thesis, State University of New York at Stony Brook 1979 (unpublished).

⁷K. Ueno *et al.*, Phys. Rev. Lett. **42**, 486 (1979).

⁸S. D. Drell and T.-M. Yan, Phys. Rev. Lett. **25**, 316 (1970); Ann. Phys. (NY) **66**, 578 (1971).

⁹J. H. Christenson *et al.*, Phys. Rev. **D8**, 2016 (1973).

¹⁰C. Chang *et al.*, Phys. Rev. Lett. **35**, 901 (1975); R. E. Taylor, in *Proceedings of the International Symposium on Lepton and Photon Interactions at High Energies Stanford, California, 1975*, edited by W. T. Kirk (SLAC, Stanford, 1976), p. 679.

¹¹H. D. Politzer, Nucl. Phys. **B129**, 301 (1977).

¹²F. Halzen and D. Scott, Phys. Rev. **D19**, 216 (1979); **18**, 3378 (1978).

¹³C. S. Lam and T. M. Yan, Phys. Lett. **71B**, 173 (1977).

¹⁴H. Fritzsche and P. Minkowski, Phys. Lett. **73B**, 80 (1978).

¹⁵C. T. Sachrajda, Phys. Lett. **73B**, 185 (1978).

¹⁶K. Kajantie, J. Lindfors, and R. Raitio, Phys. Lett. **74B**, 384 (1978).

¹⁷G. Altarelli, G. Parisi, and R. Petronzio, Phys. Lett. **76B**, 351 (1978); **76B**, 356 (1978).

¹⁸R. C. Hwa, in *Proceedings of the IX International Symposium on High Energy Multiparticle Dynamics, Tabor, Czechoslovakia, 1978* (Czechoslovak Academy of Science, Institute of Physics, Prague, 1978).

¹⁹S. Matsuda, in *Proceedings of the 19th International*

- Conference on High Energy Physics, Tokyo, 1978*, edited by S. Homma, M. Kawaguchi, and H. Miyazawa (Physical Society of Japan, Tokyo, 1979), p.221; R. C. Hwa and J. Wosiek, Rutherford Report No. RL-78-079, 1978 (unpublished).
- ²⁰E. L. Berger, Report No. SLAC-PUB-2314, 1979 (unpublished).
- ²¹R. D. Kephart *et al.*, Phys. Rev. Lett. 39, 1440 (1977); R. J. Fisk, Ph.D. thesis, State University of New York at Stony Brook, 1978 (unpublished); H. Jöstlein *et al.*, Phys. Rev. D 20, 53 (1979).
- ²²A description of an early version of the MWPC electronics is given in H. Cunitz *et al.*, Nucl. Instrum. Methods 91, 211 (1971).
- ²³V. L. Highland, Nucl. Instrum. Methods 129, 497 (1975).
- ²⁴Y.-S. Tsai, Rev. Mod. Phys. 46, 815 (1974).
- ²⁵This value was measured at Brookhaven National Laboratory by J. Hudis *et al.*, Phys. Rev. 129, 434 (1963). A recent measurement at Fermilab by S. Baker *et al.* (unpublished) yielded 3.8 mb. A recent CERN report [A. Chapman-Hatchett *et al.*, Report No. SPS/ABT/Int 79-1, 1979 (unpublished)] gives a value of 3.96 ± 0.10 mb, in agreement with Baker *et al.* If the number of Baker *et al.* were used, our cross sections would increase by 9%. In order to maintain continuity with earlier Fermilab experiments, we have used the BNL cross section.
- ²⁶E. Fermi, *Nuclear Physics* (University of Chicago Press, Chicago, 1950), p. 159.
- ²⁷P. A. Piroué and J. S. Smith, Phys. Rev. 148, 1315 (1966).
- ²⁸J. W. Cronin *et al.*, Phys. Rev. D 11, 3105 (1975); L. Kluberg *et al.*, Phys. Rev. Lett. 38, 670 (1977).
- ²⁹R. L. McCarthy *et al.*, Phys. Rev. Lett. 40, 213 (1978).
- ³⁰A. Soni, Phys. Rev. D 8, 2264 (1973).
- ³¹R. J. Oakes, Nuovo Cimento 44A, 440 (1966).
- ³²J. C. Collins and D. E. Soper, Phys. Rev. D 16, 2219 (1977).
- ³³S. Childress *et al.*, paper No. 674 submitted to 19th International Conference on High Energy Physics, Tokyo, 1978 (unpublished).
- ³⁴G. E. Hogan *et al.*, Phys. Rev. Lett. 42, 948 (1979).
- ³⁵The isotropic decay p_t acceptance is larger than the $1 + \cos^2\theta_D$ acceptance by 30% at small p_t . This decreases to 5% at $p_t = 5$ GeV/c.
- ³⁶We are indebted to J. Rutherford for this suggestion.
- ³⁷The normalization of the data presented here differs from our previous publications (Refs. 3-5). The primary cause of this change was the discovery that the target used in data set I had partially melted. Other causes are changes in the decay-angle distributions assumed in calculating the acceptance and the inclusion of nucleon motion and radiative corrections.
- ³⁸A. L. S. Angelis *et al.*, report presented at the 1979 International Symposium on Lepton and Photon Interactions at High Energies, Fermilab (unpublished); U. Becker *et al.*, report presented at European Physical Society International Conference on High Energy Physics, Geneva, 1979 (unpublished); J. Pilcher, in *Proceedings of the 1979 International Symposium on Leptons and Photons Interactions at High Energies*, edited by T. B. W. Kirk and H. D. I. Abarbanel (Fermilab, Batavia, Illinois, 1979).
- ³⁹J. G. Branson *et al.*, Phys. Rev. Lett. 38, 1334 (1977).
- ⁴⁰B. A. Gordon *et al.*, Phys. Rev. Lett. 41, 615 (1978).
- ⁴¹J. G. H. de Groot *et al.*, Z. Phys. C 1, 143 (1979).
- ⁴²P. C. Bosetti *et al.*, Phys. Lett. 70B, 273 (1977).
- ⁴³A. Benvenuti *et al.*, Phys. Rev. Lett. 42, 1317 (1979).
- ⁴⁴J. F. Owens and E. Reya, Phys. Rev. D 17, 3003 (1978).
- ⁴⁵Y. L. Dokhitzer, D. J. Dyakanov, and S. I. Trojan, Proceedings of the 13th Leningrad Winter School, SLAC Trans. No. 183, 1978 (unpublished), p. 1.
- ⁴⁶B. A. Gordon *et al.*, Phys. Rev. D 20, 2645 (1979); we use the fit for $R = 0.52$.
- ⁴⁷W. B. Atwood, Ph.D. thesis, Stanford University, SLAC Report No. 185, 1975 (unpublished); A. Bodek *et al.*, Phys. Rev. Lett. 30, 1087 (1973).
- ⁴⁸R. P. Feynman and R. D. Field, Phys. Rev. D 15, 2590 (1977).
- ⁴⁹D. A. Ross and C. T. Sachrajda, Nucl. Phys. B149, 497 (1979).
- ⁵⁰F. Sciulli, in *Proceedings of the International Symposium on Lepton and Photon Interactions at High Energies, Hamburg, 1977*, edited by F. Gutbrod (DESY, Hamburg, 1977), p. 239.
- ⁵¹W. Kienzle *et al.*, report presented at the 1979 International Symposium on Lepton and Photon Interactions at High Energies, Fermilab (unpublished); M. A. Abolins *et al.*, report presented at the European Physical Society International Conference on High Energy Physics, Geneva, 1979 (unpublished).
- ⁵²C. B. Newman *et al.*, Phys. Rev. Lett. 42, 951 (1979).
- ⁵³G. Altarelli *et al.*, Nucl. Phys. B157, 461 (1979).
- ⁵⁴J. Kripfganz, McGill University report, 1979 (unpublished).
- ⁵⁵A. P. Contogouris and S. Papadopoulos, McGill University report, 1979 (unpublished).
- ⁵⁶S. Adler, Phys. Rev. 143, 1144 (1966).
- ⁵⁷K. Kajantie and R. Raitio, Nucl. Phys. B139, 72 (1978).